Application of environmental tracers for investigation of groundwater mean residence time and aquifer recharge in faulted–hydraulic drop alluvium aquifers

Bin Ma[1,2], Menggui Jin[1,2,3], Xing Liang[1,4], and Jing Li[1]

[1]School of Environmental Studies, China University of Geosciences, Wuhan, 430074, China
[2]State Key Laboratory of Biogeology and Environmental Geology, China University of Geosciences, Wuhan, 430074, China
[3]Laboratory of Basin Hydrology and Wetland Eco–restoration, China University of Geosciences, Wuhan, 430074, China
[4]Hubei Key Laboratory of Wetland Evolution & Ecological Restoration, China University of Geosciences, Wuhan, 430074, China

Correspondence to: Menggui Jin (mgjin@cug.edu.cn)

Abstract. Documenting groundwater residence time and the recharge source is crucial for water resource management in the alluvium aquifers of arid basins. Environmental tracers (CFCs, ^{3}H, ^{14}C, $\delta^{2}H$, $\delta^{18}O$) and groundwater hydrochemical components are used for assessing groundwater mean residence times (MRTs) and aquifer recharge in faulted–hydraulic drop alluvium aquifers in the Manas River Basin (China). The very high ^{3}H activity (41.1–60 TU) in the groundwater in the Manas River upstream (south of the fault) indicates rainfall recharge during the nuclear bomb tests (since the 1960s). Carbon–14 groundwater age increases with distance (3000–5000 yrs in the midstream to > 7000 yrs in the downstream) and depth, as well as with decreasing ^{3}H activity (1.1 TU) and $\delta^{18}O$ values, confirming that the deeper groundwater is derived from paleometeoric recharge in the semi–confined groundwater system. MRTs estimated using an exponential–piston flow model vary from 19 to 101 yrs for CFCs and from 19 to 158 yrs for ^{3}H; MRTs for ^{3}H are much longer than those for CFCs probably due to the time lag (liquid vs. gas phase) through the thick unsaturated zone. The remarkable correlations between CFCs rather than ^{3}H MRTs and pH, SiO_2, and SO_4^{2-} concentrations allow estimating first–order proxies of MRTs for groundwater at different times. Relatively modern recharge is found in the south of the fault with young (post–1940) water fractions of 87–100 %, whereas in the north of the fault in the midstream area the young, water fractions vary from 12 to 91 % based on the CFC binary mixing method. This study shows that the combination of CFCs and ^{3}H residence time tracers can help analyse groundwater MRTs and identify the recharge sources for the different mixing end–members.

1 Introduction

Groundwater is the world's largest freshwater resource, supplies freshwater to billions of people, and plays a central role in energy and food security, human health, and ecosystems (Gleeson et al., 2016). Documenting the residence time of groundwater (i.e. time from recharge to drainage in pumping wells, springs, or streams) reveals information about water

storage, mixing, and transport in subsurface water systems (Cartwright et al., 2017; Dreuzy and Ginn, 2016; McGuire and McDonnell, 2006). This is particularly crucial in alluvium aquifers where fresh groundwater renewability is generally strong (Huang et al., 2017), thus functioning as potable water resources in the arid areas; also, alluvium aquifers are more vulnerable to anthropogenic contaminants and land–use changes (Morgenstern and Daughney, 2012).

Because the residence time distribution in subsurface water systems cannot be empirically measured, a commonly used approach is parametric fitting of trial distributions to chemical concentrations (Leray et al., 2016; Suckow, 2014). The widely used lumped–parameter models (LPMs; Małoszewski and Zuber, 1982; Jurgens et al., 2012), which commonly assume that the hydrologic system is at a steady–state, have been applied to subsurface water systems containing young water with modern tracers of variable input concentrations (e.g. seasonably variable stable isotope ^{2}H and ^{18}O, tritium, and ^{85}Kr; Cartwright et al., 2018; McGuire et al., 2005; Morgenstern et al., 2015; Stewart et al., 2010). The groundwater residence time tracers can be classified into three types depending on their time span. First, isotopes of water (^{18}O, ^{2}H, ^{3}H) are ideal tracers for determining the mean residence times (MRTs) shorter than approximately 5 yrs with stable isotopes (Kirchner et al., 2010; McGuire et al., 2005; Stewart et al., 2010) and up to approximately 100 yrs with ^{3}H (Beyer et al., 2016; Cartwright and Morgenstern, 2015, 2016; Morgenstern et al., 2010). Second, radioactive solute tracers such as ^{14}C, ^{36}Cl, and noble gases (^{4}He, ^{85}Kr, ^{39}Ar, and ^{81}Kr), as well as the atmospheric concentrations of synthetic organic compounds (chlorofluorocarbons, CFC–11, CFC–12, and CFC–113; and sulfur hexafluoride, SF_6), are used in determining groundwater MRTs with a much wider time span (decades to hundred millenniums) due to the radioisotopes long half–lives (Aggarwal, 2013). Third, concentrations of major ions such as inert chloride (Cl) ions determine MRTs in a similar way to the stable isotopes depending on the damping of seasonal variation input cycles that pass through a system into the output. MRTs determined through the seasonal tracer cycle method (e.g., stable isotope values or Cl concentrations), which requires detailed time series measurements, such as weekly or more frequent, may be more appropriate for water drainage through catchment and discharging into stream (Hrachowitz et al., 2009; Kirchner et al., 2010; McGuire et al., 2005) than for a groundwater system. Nevertheless, a strong correlation of major ion concentrations with groundwater age enables hydrochemistry to be used as proxy for or complementary to age via previously established relationships in closed lithological conditions (Beyer et al., 2016; Morgenstern et al., 2010, 2015).

The only true age for water is ^{3}H, a component of the water molecule with a half–life of 12.32 yrs (Tadros et al., 2014). The Northern Hemispheric ^{3}H activity is several orders of magnitude higher than that in the Southern Hemisphere (Clark and Fritz, 1997; Tadros et al., 2014) due to the atmospheric thermonuclear tests in the Northern Hemisphere in 1950s and 1960s, which resulted in mean annual ^{3}H activity peaks reaching several hundred times the natural levels in the Northern Hemisphere. The present–day rainfall ^{3}H activity in the Northern Hemisphere is still affected by the tail–end of the bomb–pulse, and it is particularly high in the arid regions of Northwest China due to both the continental effect (Tadros et al., 2014) and the China atmospheric nuclear tests from 1964 to 1974. Thus, measurement of a single sample of ^{3}H activity does not accurately assess the groundwater MRTs in the Northern Hemisphere (Cook et al., 2017), and time–series ^{3}H measurements with LPMs are required (Han et al., 2007; Han et al., 2015).

In contrast to ^{3}H, CFCs degrade slowly in the atmosphere and have relatively long degradation half–lives, which permits their uniform atmospheric distributions over large areas. However, there is 1–2 yrs lag for the Southern Hemisphere compared with the Northern Hemisphere (Cartwright et al., 2017; Cook et al., 2017; Darling et al., 2012). The build–up of CFCs in the atmosphere after the 1950s coupled with their solubility (despite low solubility) in water enables them to be commonly used as indicators of groundwater MRTs up to approximately 60 yrs (Darling et al., 2012; Han et al., 2012). Although the atmospheric concentrations of CFC–11, CFC–12, and CFC–113 have declined between 1994 and 2002 (different CFCs peaked at different times; Cook et al., 2017) thereby leaving room for ambiguity in the CFC ratio plots (Darling et al., 2012) the different atmospheric CFC ratios between today and pre–1990s (Plummer et al., 2006b) enable determination of groundwater MRTs using CFCs. Consequently, CFCs have been commonly viewed as alternatives to ^{3}H for calculating groundwater MRTs with the decline in the bomb–pulse ^{3}H activity (Cartwright et al., 2017; Cook et al., 2017; Qin et al., 2011). However, groundwater MRTs may not be always be accurate when calculated using CFCs: for example, MRTs are much lower than the actual values if CFC inputs are entrapped excess air in the unsaturated zone during recharge (Cook et al., 2006; Darling et al., 2012) or contaminated in urban and industrial environments (Carlson et al., 2011; Han et al., 2007; Mahlknecht et al., 2017; Qin et al., 2007), and are much higher if CFC inputs are degraded in anaerobic groundwater (most notably CFC–11 and CFC–113; Cook and Solomon, 1995; Horneman et al., 2008; Plummer et al., 2006b).

Additionally, mixing between water of different ages, which occurs both within the aquifer and pumping from long–screened wells (Cook et al., 2017; Custodio et al., 2018; Visser et al., 2013), poses difficulties for estimating MRTs using tracer data. The calculated MRTs will be less than the actual values in mixed water due to aggregation errors (Cartwright and Morgenstern, 2016; Kirchner, 2016; Stewart et al., 2017). MRT estimation using a multi–model approach based on incorporated residence time tracers should reduce the calculation uncertainty (Green et al., 2016; Visser et al., 2013) and indicate whether MRTs can be realistically estimated (Cartwright et al., 2017).

The hypothesis mixing within the aquifers and pumping from the long–screened wells is common in the faulted–hydraulic drop alluvium aquifers of the Manas River Basin (MRB) in the arid regions of Northwest China (Fig. 1). In particular, pumping from long–screened wells (of which there are over 10 000 boreholes, Ma et al., 2018) makes groundwater mixing most likely. MRTs that result from a deep unsaturated zone (with a water table depth of 180 m) and contrasting geological settings (a level difference of 130 m hydraulic drop caused by the thrust fault) are still insufficiently recognised in the alluvium aquifer (Fig. 1c). We aim to provide the first estimation of the MRTs of borehole groundwater drainage (e.g., well withdrawal) using CFC and ^{3}H concentrations. We then analyse the major hydrochemical ions in groundwater as first–order proxies for MRTs. In addition, we identify the recharge sources for the different mixing end–members and constrain mixing rates.

2 Geological and hydrogeological setting

The bedrock of the upper Manas River catchment in the mountain area consists of granites, sedimentary formations of Devonian and Carboniferous age, and Mesozoic limestone (Jelinowska et al. 1995). Pyroclastic rock is exposed in relatively small areas in the south mountain. The piedmont and oasis plains are filled with Cenozoic strata, including the Tertiary and Quaternary deposits with a total depth more than 5000 m in the piedmont area and decreasing to 500–1000 m in the centre of the plain (Zhao 2010). The vertical cross section (Fig. 1c) shows that the Quaternary deposits consist of pebbles, sandy gravel, and sand in the piedmont plain. The clay content in the Quaternary deposits increases from the overflow spring zone to the north oasis plain, which consists of silty loam and clay. The Huoerguosi–Manas–Tugulu thrust faults occurred in the early Pleistocene and cut the Tertiary strata with a total length of approximately 100 km in the piedmont alluvial fan (Fig. 1), which are water block features. These faults were intermittently active from the middle late–Pleistocene and then tended to be more active from the late Holocene (Cui et al., 2007).

In the mountain area, groundwater consists of metamorphic rock fissure water, magmatic rock fissure water, clastic rock fissure water and Tertiary clastic rock fissure water (Cui et al., 2007; Zhou, 1992). In the piedmont plain of Shihezi (SHZ) zone, groundwater is from a single–layer unconfined aquifer. From the overflow spring zone to the central oasis plain, groundwater consists of shallow unconfined water and deep confined water. The hydraulic gradient, hydraulic conductivity and transmissivity show a large range of variations due to changes in grain size and local increases of clay content (Wu 2007). The groundwater flow direction is consistent with the Manas River flow direction. In the piedmont plain, the aquifer is recharged by the Manas River water and unconfined with saturated thickness more than 650 m, and is hydraulically connected to the hydrological network in the piedmont plain and north oasis plain (Ma et al., 2018; Wu 2007). The piedmont plain unconfined aquifer depth decreases gradually from south to north and has relatively fresh groundwater with TDS of < 1 g L^{-1}. Groundwater discharges via springs in the north area of SHZ (Fig. 1c). The shallow unconfined groundwater in the north oasis plain has TDS of > 3 g L^{-1}, and the underlying confined groundwater show relatively fresh water with TDS of 0.3–1.0 g L^{-1} (Wu 2007). The water table depth is as deep as 180 m and a level difference of 130 m hydraulic drop is observed due to the thrust fault in the south margin in SHZ (Fig. 1c).

3 Materials and methods

3.1 Water sampling

In total, 29 groundwater (pumped from fully penetrating well, of which 3 are from spring and 3 are from the artesian well) were collected along the Manas River during June to August, 2015 (from G1 to G29 in Table 1 and Fig. 2). Groundwater were separated into three clusters including the upstream groundwater (UG, south of the Wuyi Road), midstream groundwater (MG, area between the Wuyi Road and the West Main Canal–Yisiqi), and downstream groundwater (north of the West Main Canal–Yisiqi) based on the hydrochemistry and stable isotope data. Groundwater were sampled from wells

for irrigation and domestic supply, in which shallow wells were pumped for a minimum 5 min before sampling and deep wells were active for irrigation for more than 10 days prior to the sampling. Surface water samples (river water, ditch and reservoir water) and groundwater samples data from G30 to G39 were reported by Ji (2016) and Ma et al. (2018).

Water temperature (T), pH values, electrical conductivity (EC) and dissolved oxygen (DO) were measured (Table 1) in the field using calibrated Hach (HQ40d) conductivity and pH meters, which had been calibrated before use. Bicarbonate was determined by titration with 0.05 N HCl on site. Samples to be analyzed for chemical and stable isotopic values were filtered on site through 0.45 μm millipore syringe filters and stored in pre–cleaned polypropylene bottles at 4 ºC until analysis. For cation and strontium isotope analysis, the samples were acidified to pH < 2 with ultrapure HNO_3.

Extreme precautions are needed to be taken to avoid contamination from equipment such as pumps and tubing (Cook et al., 2017; Darling et al., 2012; Han et al., 2012) for CFCs samples. After purging the wells, water samples were collected directly from the borehole using a copper tube sampling pipe for CFC analysis. One end of the pipe was connected to the well casing, and the other end was placed in the bottom of a 120 mL borosilicate glass bottle, inside a 2000 mL beaker. The well water was allowed to flow through the tubing for ten minutes, thoroughly flushing the tubing with well water. The bottle was submerged, filled and capped underwater when there was no bubbles appeared in the bottle, following the protocols described by Han et al. (2007). In this study, 5 bottles were collected at each well and 3 of which were analyzed. A total of 10 wells were collected for CFC (CFC–11, CFC–12 and CFC–113) analysis. Unfiltered samples for ^{3}H analysis were collected and stored in 500 mL airtight polypropylene bottles. Dissolved inorganic carbon (DIC) for ^{14}C activity analysis was precipitated in field from 180 to 240 L water samples to $BaCO_3$ by addition of excess $BaCl_2$ previously brought to pH ≥ 12 by addition of NaOH, which then were sealed in 500 mL polypropylene bottles, following the procedure reported by Chen et al. (2003).

3.2 Analytical techniques

The CFC concentrations were analysed within 1 month of sample collection at the Groundwater Dating Laboratory of the Institute of Geology and Geophysics, Chinese Academy of Sciences (IGG–CAS) using a purge–and trap gas chromatography procedure with an Electron Capture Detector (ECD), which has been reported by Han et al. (2012, 2015) and Qin et al. (2011). The procedures were after by Oster et al. (1996). The detection limit for each CFC is about 0.01 pmol L^{-1} of water, with the error less than ±5 %. The obtained results are shown in Table 1.

The ^{3}H and ^{14}C activities of groundwater were measured using liquid scintillation spectrometry (1220 Quantulus ultra–low–level counters, PerkinElmer, Waltham, MA, USA) at the State Key Laboratory of Biogeology and Environmental Geology, China University of Geosciences in Wuhan. Water samples for ^{3}H were distilled and electrolytically enriched prior to being analysed. Detailed procedures were after by Morgenstern and Taylor (2009). ^{3}H activities were expressed as tritium unit (TU), with 1 TU corresponding to a $^{3}H/^{1}H$ ratio of 1×10^{-18}. For ^{14}C samples, the obtained $BaCO_3$ samples were first converted to CO_2, then to acetylene (C_2H_2) which in turn was trimerized catalytically to C_6H_6 as described by Polach (1987),

prior to being analysed. ^{14}C activities were reported as percent modern carbon (pMC). The achieved precision for ^{3}H and ^{14}C were ±0.2 TU and ±0.4 pMC respectively.

The cation, anion and stable isotope measurements were performed at the State Key Laboratory of Biogeology and Environmental Geology, China University of Geosciences in Wuhan. Cations were analysed using an inductively coupled plasma atomic emission spectrometry (ICP–AES) (IRIS Intrepid II XSP, Thermo Elemental). Anions were analysed on filtered unacidified samples using ion chromatography (IC) (Metrohm 761 Compact IC). Analytical errors were inferred from the mass balance between cations and anions (with HCO_3), and are within ±6 %. Stable isotopic values (δ^2H and $\delta^{18}O$) analyses were measured using a Finnigan MAT–253 mass spectrometer (Thermo Fisher, USA, manufactured in Bremen, Germany), with the TC/EA method. The δ^2H and $\delta^{18}O$ values (Table 1) were presented in δ notation in ‰ with respect to the Vienna Standard Mean Ocean Water (VSMOW), with an analytical precision of 0.5 ‰ vs. VSMOW for δ^2H and of 0.1 ‰ for $\delta^{18}O$.

3.3 Groundwater dating

3.3.1 CFCs indicating modern water recharge

Knowledge of the history of the local atmospheric mixing ratios of CFCs in precipitation is first required for indicating modern water recharge. The difference between the local and global background atmospheric mixing ratios of CFCs in the Northern Hemisphere – *CFC excess* – varies substantially based on the industrial development. Elevated CFC concentrations (10–15 % higher than those of the Northern Hemisphere) have been reported in the air of urban environments such as Las Vegas, Tucson, Vienna, and Beijing (Barletta et al., 2006; Carlson et al., 2011; Han et al., 2007; Qin et al., 2007), whereas in Lanzhou and Yinchuan (Northwest China) they were approximately 10 % lower (Barletta et al., 2006). Manas River Basin is located in Northwest China (Fig. 1a), has a very low population density, and is far from industrial cities. To evaluate CFC ages, the time series trend of Northern Hemisphere atmospheric mixing ratio (Fig. 3; 1940–2014, http://water.usgs.gov/lab/software/air/cure/) was adopted in this study.

Measured CFC concentrations (in pmol L^{-1}) can be interpreted in terms of partial pressures of CFCs (in pptv) in solubility equilibrium with the water sample based on Henry's law. Concrete computational process was conducted following Plummer et al. (2006a). In arid Northwest China, estimating the local shallow groundwater temperature as recharge temperature is more suitable than the annual mean surface air temperature (Qin et al., 2011) because the local low precipitation usually cannot reach the groundwater. Studies On the MRB (Ji, 2016; Wu, 2007) have also indicated much less vertical recharge water from the local precipitation compared with abundant groundwater lateral flow recharge and river leakage from the mountain to the piedmont areas. In this study, the measured groundwater temperature, which varied from 11.5 to 15.7 ºC between wells (Table 1), was used as the recharge temperature to estimate the groundwater input CFC concentrations. Surface elevations of the recharge area vary from 316 to 755 m. The modern water recharge was then

190 determined by comparing the calculated partial pressures of CFCs in solubility equilibrium with the water samples with historical CFC concentrations in the air (Fig. 3).

3.3.2 The apparent ^{14}C ages

Carbon–14 (^{14}C, half–life: 5730 yrs) activity in groundwater is often used to estimate groundwater age over time periods of approximately 200 and 30 000 yrs, and to determine the recharge from mixing water in various climate conditions (Cook, et
195 al., 2017; Custodio et al., 2018; Huang et al., 2017). Calculation of ^{14}C groundwater age may be complicated if dissolved inorganic carbon is derived from a mixture of sources or ^{14}C originating from the atmosphere or soil zone is significantly diluted by the dissolution of ^{14}C–free carbonate minerals in the aquifer matrix and biochemical reactions along the groundwater flow paths (Clark and Fritz, 1997). Although only minor carbonate dissolution is likely, determination of groundwater residence times requires ^{14}C correction (Atkinson et al., 2014). When the dissolution of carbonate during
200 recharge or along the groundwater flow path may dilute the initial soil CO_2, $\delta^{13}C$ can be used to trace the process (Clark and Fritz, 1997). An equation for the reaction between CO_2–containing water with a carbonate mineral is commonly written as follows (modified after Pearson and Hanshaw, 1970):

$$CO_2 + H_2O + CaCO_3(\delta^{13}C_{carb} = 0) \rightarrow Ca^{2+} + 2HCO_3^-(\delta^{13}C_{DIC}), \quad \text{(R1)}$$

where $\delta^{13}C_{carb}$ is the dissolved carbonate $\delta^{13}C$ value (approximately 0; Clark and Fritz, 1997), and $\delta^{13}C_{DIC}$ is the measured
205 $\delta^{13}C$ value in groundwater.

Depending on knowing the measured ^{14}C activity after adjustment for the geochemical and physical dilution processes in the aquifer (without radioactive decay), the groundwater apparent ^{14}C ages (t) can be calculated from the following decay equation:

$$t = -\frac{1}{\lambda_{^{14}C}} \times \ln \frac{a^{14}C}{a_0{}^{14}C}, \quad (1)$$

210 where $\lambda_{^{14}C}$ is the ^{14}C decay constant ($\lambda_{^{14}C} = \ln 2/5730$), and $a^{14}C$ is the measured ^{14}C activity of the DIC in groundwater. As mentioned above, the estimated ages are really apparent ages due to the mixture of waters with wide range of ages (Custodio et al., 2018; Suckow, 2014).

Previous studies in the arid northwest China (Edmunds et al., 2006; Huang et al., 2017) have concluded that a volumetric value of 20 % “dead” carbon derived from the aquifer matrix was recognized, which is consistent with the value (10–25 %)
215 obtained by Vogel (1970). Therefore, the initial ^{14}C activity ($a_0{}^{14}C$) of 80 pMC is used to correct groundwater ^{14}C ages (results are shown in Table 1), despite this simple correction makes no attempt to correct the age of individual samples that may have experienced different water–rock interaction histories.

3.3.3 Groundwater mean residence time estimation

Groundwater mixing may occur both within the aquifer and in the long–screened wells (Cook et al., 2017; Custodio et al., 2018; Visser et al., 2013). The groundwater residence times (ages) often display a wide range because recharge occurs under various climate conditions (Custodio et al., 2018). With the aid of gaseous tracers (e.g. ^{3}H, CFCs, SF_6 and ^{85}Kr) one can describe the mixing distribution using a mixing model (Stewart et al., 2017; Zuber et al., 2005) to obtain the groundwater MRTs. LPMs is an alternative approach to interpret MRTs for water flow through the subsurface systems to the output. For the steady–state subsurface hydrologic system, ^{3}H and CFCs tracers entering groundwater with precipitation are injected proportionally to the volumetric flow rates by natural processes; the output concentration in water at the time of sampling relating to the input ^{3}H and CFCs can be described by the following convolution integrals (Małoszewski and Zuber, 1982):

$$C_{\text{out}}(t) = \int_0^{\infty} C_{\text{in}}(t-\tau)\, g(\tau) e^{-\lambda_{^3\text{H}} \tau} \mathrm{d}\tau \qquad \text{for } ^{3}\text{H tracer} \tag{2a}$$

$$C_{\text{out}}(t) = \int_0^{\infty} C_{\text{in}}(t-\tau)\, g(\tau) \mathrm{d}\tau \qquad \text{for CFCs tracer}, \tag{2b}$$

where C_{out} is the tracer output concentration, C_{in} is the tracer input concentration, τ is the residence time, $t-\tau$ is the time when water entered the catchment, $\lambda_{^3\text{H}}$ is the ^{3}H decay constant ($\lambda_{^3\text{H}} = \ln 2/12.32$), and $g(\tau)$ is the system response function that describes the residence time distributions (RTDs) in the subsurface hydrologic system.

In this study, the CFC concentrations from the time series trend of the Northern Hemisphere atmospheric mixing ratio (Fig. 3) and ^{3}H concentrations in precipitation in Urumqi (Fig. 4) are treated as proxies for CFC and ^{3}H recharge concentrations (C_{in}), respectively. The historical precipitation ^{3}H activity in the Urumqi station (Fig. 4) is reconstructed with the data available from the International Atomic Energy Agency (IAEA) using a logarithmic interpolation method. The precipitation ^{3}H activity between 1969 and 1983 at Hong Kong and Irkutsk with different latitudes are used (data is available at <https://www.iaea.org/>). The time series of ^{3}H activity (Fig. 4) was used as the input data are based on the following considerations. First, the MRB is located in the Northern Hemisphere, where the bomb–pulse ^{3}H activity is several orders of magnitude higher than in the Southern Hemisphere (Clark and Fritz, 1997; Tadros et al., 2014) and was superimposed with the China atmospheric nuclear tests from 1964 to 1974 in the arid regions of Northwest China; thus, the remnant ^{3}H activity remains affected by the tail–end of the bomb pulse. Second, the study area is more than 3500 km away from the western Pacific, where the atmospheric ^{3}H activity is much higher than that at coastal sites due to the continental effect (Tadros et al., 2014). Furthermore, although the atmospheric ^{3}H activity varies between seasons (Cartwright and Morgenstern, 2016; Morgenstern et al., 2010; Tadros et al., 2014), the mean annual values (Fig. 4) were considered in this study.

Several RTDs have been described (Małoszewski and Zuber, 1982; Jurgens et al., 2012) and have been widely used in studies of variable timescales and catchment areas (Cartwright and Morgenstern, 2015, 2016; Cartwright et al., 2018; Hrachowitz et al., 2009; Morgenstern et al., 2010, 2015; McGuire et al., 2005). The selection of each model depends on the

hydrogeological situations in the hydrologic system to which it is applicable. The exponential–piston flow model (EPM) describes an aquifer that contain a segment of the exponential flow followed by a segment of piston flow. The piston flow model assumes minimal water mixing from different flow lines and little or no recharge in the confined aquifer; the exponential flow model assumes a full mixing of water in the unconfined aquifer and the receipt of areally distributed recharge (Jurgens et al., 2012; Małoszewski and Zuber, 1982). The weighting function of this model is given by

$$g(\tau) = 0 \qquad \text{for} \quad \tau < \tau_m (1 - 1/\eta) \tag{3a}$$

$$g(\tau) = \frac{\eta}{\tau_m} e^{(-\eta\tau/\tau_m + \eta - 1)} \qquad \text{for} \quad \tau \geq \tau_m (1 - 1/\eta) \tag{3b}$$

The dispersion model (DM) mainly measures the relative importance of dispersion to advection, and is applicable for confined or partially confined aquifers (Małoszewski, 2000). Its RTD is given by

$$g(\tau) = \frac{1}{\tau\sqrt{4\pi D_p \tau/\tau_m}} e^{-\left(\frac{(1-\tau/\tau_m)^2}{4\pi D_p \tau/\tau_m}\right)} \tag{4}$$

The weighting function of the exponential mixing model (EMM) is

$$g(\tau) = \frac{1}{\tau_m} e^{(-\tau/\tau_m)}, \tag{5}$$

where τ_m is the mean residence time, η is the ratio defined as $\eta = (l_P + l_E)/l_E = l_P/l_E + 1$, where l_E (or l_P) is the length of area at the water table (or not) receiving recharge, D_p is the dispersion parameter, which is the reciprocal of the Peclet number (*Pe*) and defined as $D_p = D/(vx)$, where D is the dispersion coefficient ($m^2\,day^{-1}$), v is velocity ($m\,day^{-1}$), and x is distance (m).

Each RTD has one or two parameters, MRT (τ_m) is determined by convoluting the input (the time series ^3H and CFCs input in rainfall) to each model to match the output (the measured ^3H and CFC concentrations in groundwater), and other parameters (η and D_p) are determined depending on the hydrogeological conditions. To interpret the ages of the MRB data set, EPM (η=1.5 and 2.2), DM (D_p=0.03 and 0.1), and EMM models were used, after which MRTs with different RTDs were cross–referenced.

4 Results and discussion

4.1 Stable isotope and major ion hydrochemistry

The δ^2H and $\delta^{18}O$ values in the study area vary from –75.88 to –53.40 ‰ and –11.62 to –6.76 ‰ for the surface water, and from –82.45 to –62.16 ‰ and –12.19 to –9.01 ‰ for the groundwater. Figure 5a shows the δ^2H and $\delta^{18}O$ values of surface water and groundwater in relation to the precipitation isotopes of the closest GNIP station (Urumqi station in Fig. 1a). Both the linear slope (7.3) and intercept (3.1) of the Local Meteoric Water Line (LMWL) are lower than that of the Global

Meteoric Water Line (GMWL, 8 and 10, respectively; Craig 1961). Surface water (ditch, river and reservoir water) are more enriched in heavy isotopes and defined an evaporation line with a slope of 4.5 (Fig. 5b), which is much higher than that solely calculated from the upstream river water and reservoir water (slope=3.2 from Ma et al., 2018).

Groundwater deuterium excess values ($d-\text{excess}=\delta^{2}\text{H}-8\delta^{18}\text{O}$, Fig. 5b) defined by Dansgaard (1964) lie close to the annual mean LMWL (d_{LMWL}=13 ‰), which also suggest little isotope fractionation by evaporation as *d*–excess value decreases when water evaporates (Han et al. 2011; Ma et al., 2015). The *d*–excess values of surface water decrease from 17.12 ‰ in the upstream area to 0.68 ‰ in the downstream area, indicating strong evaporation effect, which is also demonstrated by the low slope (evaporation slope=4.5) of the surface waters. A recent study (Benettin et al., 2018) indicated that the evaporation line obtained from various sources of water is often not the true evaporation line. All samples of surface water in the present study were collected in the summer of 2015 and were recharged from the mountain areas in the same season. Although they were collected from different areas (ditch water, reservoir water, and Manas River water), the linear trend obtained may have implications for surface water evaporation.

The hydrochemistry compositions of surface water and groundwater in the MRB reflect the evolution from the fresh HCO_3–SO_4–Ca water type to the HCO_3–SO_4–Na–Ca type and further to the HCO_3–SO_4–Na type, and finally to the brine Cl–SO_4–Na water type along the groundwater flow paths (Fig. 6). Groundwater in the unconfined aquifers (e.g., intermountain depression and piedmont plain aquifers in Fig. 1c) is dominated by Ca^{2+} and HCO_3^- with a relatively low concentration of Na^+ (Fig. 6). Groundwater in the confined aquifers is characterised by a wide range with progressively increasing Na^+ and Cl^- ions, whereas Ca^{2+} and Mg^{2+} ions decrease progressively towards the more concentrated end of the salinity spectrum (Fig. 6). The concentration of SO_4^{2-} ion gradually increases in the unconfined aquifers and becomes less dominant in the confined aquifers along the groundwater flow paths (Fig. 6).

4.2 Modern and paleo–meteoric recharge features

4.2.1 Stable isotope indications

Stable isotopes (δ^2H and δ^{18}O), components of the water molecule that record the atmospheric conditions at the time of recharge (Batlle–Aguilar et al., 2017; Chen et al., 2003), provide valuable information on groundwater recharge processes. Generally, there are two possible meteoric recharge sources including precipitation in the modern climate and in the paleoclimate. Groundwater whose isotopic values are more depleted than the modern precipitation usually would be ascribed to two recharge sources including snowmelt/precipitation at higher elevation and precipitation fallen during cooler climate. Figure 5 shows that groundwater generally lie along the LMWL but do not define evaporation trend, implying little evaporation and isotope exchange between groundwater and the rock matrix have occurred (Ma et al., 2018; Négrel et al., 2016). Transpiration over evaporation is likely to be dominant in the soil when infiltration as soil water uptake by root is not significantly isotope fractionated (Dawson and Ehleringer 1991).

Three groundwater clusters can be identified in the δ^2H–$\delta^{18}O$ plot (Fig. 5b), suggesting different recharge sources among the upstream, midstream, and downstream areas. The first group with average δ^2H and $\delta^{18}O$ values of –68.24 and –10.08 ‰, respectively, was from UG and is located much closer to the summer rainfall (Fig. 5a), reflecting more enriched summer rainfall inputs. Negligible evaporation trends were observed in UG, although the recharge was mostly in the summer due to the fast river leakage in the intermountain depression through highly permeable pebbles and gravel deposits (Fig. 1c). Furthermore, the detectable CFC concentrations and high ^3H activity (Table 1) also indicate a modern precipitation recharge. An overlap between surface water and UG indicates the same recharge sources, because some alignment of river water and groundwater isotopic values suggest a qualitative recharge under climate conditions similar to contemporary conditions (Huang et al., 2017).

The second group with average δ^2H and $\delta^{18}O$ values of –73.10 and –11.0 ‰, respectively, overlapped with the annual amount–weighted mean rainfall isotopic value from MG. Such isotopic values are comparable to the modern annual amount–weighted mean rainfall δ^2H and $\delta^{18}O$ values (–74.7 and –11.0 ‰, respectively; Fig. 5a), probably reflecting annual modern precipitation recharge. Another explanation for the relatively highly scattered MG isotopic values in the δ^2H–$\delta^{18}O$ plot (Fig. 5b) is mixing with different time–scale recharges of variable isotopic values at different aquifers and sites along the groundwater flow paths. Groundwater isotopes in the piedmont plain are relatively rich in heavy isotopes (Fig. 5b), which overlap with the river water, indicating fast river leakage recharge in a short time (Ma et al., 2018). Groundwater isotopes in the oasis plain diverge from those in the piedmont plain (Fig. 5b) and do not align with surface water, indicating recharge with longer flow paths rather than fast river leakage recharge.

The third group, the most depleted in heavy isotopes (–82.36 and –12.03 ‰), was from DG and was located much closer to the winter rainfall in the δ^2H–$\delta^{18}O$ plot (Fig. 5b). Studies (Ji, 2016; Ma et al., 2018) have shown that vertical recharge from the winter rainfall in the downstream area is unlikely. As the altitude effects of precipitation recharge (Clark and Fritz, 1997) and paleo–meteoric recharge during the cooler climate (Chen et al., 2003) could collectively account for the isotopically depleted groundwater, it is usually not easy to distinguish the precipitation recharge sources at a higher elevation from paleo–meteoric recharge. However, the positive altitude gradient of isotopes in precipitation (Kong and Pang, 2016) over North Tianshan Mountain (Fig. 1a) was attributed to moisture recycling, and sub–cloud evaporation effects would yield more enriched isotopes from higher–altitude precipitation recharge. The isotopically enriched UG (Fig. 5b) in the intermountain depression with higher altitude (Fig. 1c) was recharged from the high mountains. This also demonstrated that DG is unlikely to be from the high mountain recharge. Accordingly, its depleted isotopic values (Fig. 5b) were attributed to the paleo–meteoric recharge in a cooler climate. In the las glacial period, temperatures in Xinjiang region (Li et al., 2015) and North China Plain (Chen et al., 2003) were cooler by approximately 10 ºC and 6–9 ºC, respectively, compared with the present day. Groundwater had a depleted $\delta^{18}O$ value of –12.0 ‰ from the paleo–meteoric recharge in the arid regions of Northwest China, such as in the Minqin basin (Edmunds et al., 2006), as well as in the East (Li et al., 2015) and West (Huang et al., 2017) Junggar Basin (Fig. 1a).

4.2.2 CFCs indications

Table 1 shows that groundwater with well depths of 13–150 m contained detectable CFC concentrations (0.17–3.77 pmol L^{-1} for CFC–11, 0.19–2.18 pmol L^{-1} for CFC–12, and 0.02–0.38 pmol L^{-1} for CFC–113) in both the upstream and midstream areas, indicating at least a small fraction of young groundwater components (post–1940). The highest concentration was observed in the UG (G3), south of the fault. The median and the lowest were observed in the west and east banks, respectively, of the East Main Canal in the MG, north of the fault. In the midstream area (Fig. 2), CFC concentrations generally decreased with well depth south of the reservoirs (G25, G8, and G9), and increased with well depth north of the reservoirs (G15 and G16), which might indicate different groundwater flow paths (e.g., downward or upward flow directions).

The groundwater aerobic environment (Table 1, DO values vary from 0.7 to 9.8 mg L^{-1}) makes CFC degradation under anoxic conditions unlikely. Nevertheless, CFC–11 has shown a greater propensity for degradation and contamination than CFC–12 (Plummer et al., 2006b). Therefore, we use CFC–12 to interpret the modern groundwater recharge in the following discussions. The estimated CFC partial pressure and possible recharge year are shown in Table 2 and Fig. 3. The UG (G3) CFC–113 and CFC–12 both indicate the 1990 precipitation recharge (Table 2), probably a piston flow recharge in the upstream area. The MG CFC–11–based modern precipitation recharge was in agreement with that based on CFC–12 concentrations within 2–8 yrs, whereas the CFC–113–based recharge was as much as 4–11 yrs later than that the other two, signifying recharge of a mixture of young and old groundwater components in the midstream area. The most recent groundwater recharge was in the upstream area (G3 with 1990 rainfall recharge), which was most likely because the flow paths from recharge sources here were shorter than those of the piedmont groundwater samples in the midstream area.

G5 and G7 were located in the east bank of the East Main Canal in the midstream area and were closer than G15 and G16 north of the reservoir, showing that the modern recharge was much earlier than that of G15 and G16 (Table 2). This could be explained by the lower groundwater velocities in the east bank of the East Main Canal, where the hydraulic gradient (Fig. 2) was much smaller than that in the west. Furthermore, groundwater recharge became earlier with increasing well depth from 48 to 100 m south of the reservoir (G25, G8 and G9), whereas that north of the reservoir became later with increasing well depth from 23 to 56 m (G15 and G16; Table 2, Fig. 2). The different trends for the relationship between groundwater recharge year and well depth might be due to the different flow paths between the two sites (e.g., reservoir south and north).

Comparing CFC concentrations helps to indicate samples containing young (post–1940) and old (CFC–free) water (Han et al., 2007; Han et al., 2012; Koh et al., 2012) or exhibiting contamination or degradation (Plummer et al., 2006b). The cross–plot of the concentrations for CFC–113 and CFC–12 (Fig. 7a) demonstrates that all of the groundwater can be characterised as binary mixtures between young and older components, though there is still room for some ambiguity around the crossover in the late 1980s (Darling et al., 2012). As shown in Fig. 7a, all of the MG samples are located in the shaded region, representing no post–1989 water recharge. The UG (G3) sample is clearly relatively modern and seems to have been recharged in 1990 through piston flow or mixed with old water and post–1995 water. Using the method described by

Plummer et al. (2006b) with the binary mixing model, the fractions of young water were found to vary from 12 to 91 % (Table 2) for the MG samples with the relatively low young fractions of 12 and 18 % in the MG samples (G5 and G7) from east bank of the East Main Canal. These two well water table were deeper than 40 m, probably indicating a relatively slow and deep circulated groundwater flow. This hypothesis is also suggested by the lower DO (3.7–4.6 mg L^{-1}; Table 1) and nitrate concentrations (8.6–9.5 mg L^{-1} from Ma et al., 2018) and considerably smaller hydraulic gradient (Fig. 2). Furthermore, a fraction of young water as high as 100 % was obtained for G3 sample with the recharge water from 1990, and a 87 % fraction was obtained by from the binary mixture of post–1989 water and old water (Table 2). The relatively modern recharge for the G3 sample was likewise explained by its high DO (9.8 mg L^{-1}; Table 1) and relatively low nitrate concentration (7.9 mg L^{-1} from Ma et al., 2018), which represented the contribution of high–altitude recharge rather than the old water.

CFC contamination and sorption in the unsaturated zone during recharge considerably influenced the interpretation of groundwater recharge. Points off the curves in the cross–plot of CFC concentrations may indicate contamination from the urban air with CFCs during sampling (Carlson et al., 2011; Cook et al., 2006; Mahlknecht et al., 2017) or the degradation or sorption of CFC–11 or CFC–113 (Plummer et al., 2006b). Figure 7 demonstrates that the urban air with CFC contaminations, which generally increased CFC concentrations above the global background atmospheric CFC concentrations for the Northern Hemisphere, are unlikely. Elevated CFC concentrations have been reported in the air of urban environments such as Las Vegas, Tucson, Vienna and Beijing (Barletta et al., 2006; Carlson et al., 2011; Han et al., 2007; Qin et al., 2007) rather than in the arid regions of Northwest China (Barletta et al., 2006). Hence, the anomalous ratios of CFC–11/CFC–12 (Fig. 7b) off the model lines might be attributed to sorption in the unsaturated zone during recharge rather than the degradation of CFC–11 (Cook et al., 2006; Plummer et al., 2006b) under anoxic conditions (Table 1, DO values vary from 0.7 to 9.8 mg L^{-1}). Nevertheless, the small deviations (Fig. 7b) indicate a low sorption rate. A higher CFC sorption rate occurs with high clay fraction and high organic matter in soils (Russell and Thompson, 1983), and vice versa (Carlson et al., 2011). Therefore, the hypothesis of a low sorption rate due to the low clay fraction and low organic matter content in the intermountain depression and the piedmont plain (Fig. 1c) seems reasonable.

The time lag for CFC transport through the thick unsaturated zone (Cook and Solomon, 1995), as well as degradation, especially for CFC–11 being common in anaerobic groundwater (Horneman et al., 2008; Plummer et al., 2006b), are both important considerations when interpreting groundwater recharge using CFC concentrations. The time lag for CFC diffusions through the deep unsaturated zone in simple porous aquifers, a function of the tracer solubility in water, tracer diffusion coefficients, and soil water content (Cook and Solomon, 1995), have been widely proved (Darling et al., 2012; Qin et al., 2011). The small differences in CFC–11 and CFC–12 recharge years (Table 2) demonstrate that the time lag should be short in the faulted–hydraulic drop alluvium aquifers with the deep unsaturated zone (Fig. 1c). Studies on the MRB (Ma et al., 2018; Wang, 2007; Zhou, 1992) have shown that groundwater mainly recharged by the river fast leakage in the upstream area and piedmont plain, where the soil texture consists of pebbles and sandy gravel (Fig. 1c); this suggests that the

unsaturated zone air CFC closely follows that of the atmosphere, so the recharge time lag through the unsaturated zone is not considered.

4.2.3 ^{3}H and ^{14}C indications

Groundwater recharge was be determined using ^{14}C activity in groundwater for time intervals from centuries to millenniums (Custodio et al., 2018), and ^{3}H has been used for modern precipitation recharge, especially during the nuclear bomb periods (Cook et al., 2017; Huang et al., 2017). Groundwater ^{3}H activity varied from 60 to 1.1 TU (Fig. 4 and Table 1), with the highest value in UG (G4), followed by MG (mean 12.4 TU) and DG (mean 4.5 TU). All of the ^{3}H values in UG (G1, G2, and G4) and G23 (belonging to MG) were higher than 34.3 TU, which indicated some fractions of the 1960s precipitation recharge. Groundwater with ^{3}H activity lower than 5.6 TU contained some pre–1950s recharge.

Both ^{3}H and ^{14}C activities showed large variations with the distance to the mountainous region along groundwater flow paths in the midstream area (Fig. 8), suggesting recharge over a mixture of short to long timescales. Two different trends for the distribution of ^{3}H activity with distance to the mountainous region (Fig. 8) from the upstream to midstream areas were observed. First, increase in ^{3}H activity in groundwater in the upstream area from 41.1 (G1 and G2) to 60 TU (G4) with distance indicated a larger fraction of 1960s precipitation for G4 than for G1 and G2; indeed, as seen in Fig. 2, near G4 samples exhibited the highest hydraulic gradient values. Second, ^{3}H activity in groundwater in the midstream area showed an obvious reduction trend along the Manas River from 37.5 (G23) to 1.1 TU (G14), indicating that more fractions of pre–bomb precipitation recharge may have occurred along the groundwater flow direction in the north of the fault. Furthermore, ^{14}C activity in the MG showed small increases with distance (Fig. 8) from 43.4 to 54.6 pMC, with the exception of sample G12 at approximately 54 km (86.9 pMC with a $^{14}C_{corr}$ age of –684 yrs; modern recharge; Table 1), whereas that in the DG decreased to 23.5 pMC. The presence of detectable ^{3}H (2.9–6.91 TU) in DG with low ^{14}C values (23.5–34.3 pMC) indicated that some mixing with post–bomb precipitation recharge may have occurred.

Combined use of CFCs and ^{3}H may help resolve even more complicated recharge features due to the large difference of the temporal pattern in the input functions between CFCs and ^{3}H. Compared with plots comparing tracer ratios, tracer–tracer concentration plots have some advantages because they reflect more directly the measured quantities and potential mixtures (Plummer et al., 2006b), such as mixing with irrigation water (Han et al., 2012, 2015; Koh et al., 2012) or young water mixtures in different decades (Han et al., 2007; Qin et al., 2011). The plot of ^{3}H vs. CFC–12 (Fig. 9; CFC–11 and CFC–113 can substitute for CFC–12) shows that some samples (G9, G15 and G20) are slightly above the piston flow line, whereas in Fig. 7a they are away from the piston flow line but on the binary mixing lines. G15 and G20 had the shallowest well depths of 23 and 13 m, respectively. The G9 sample was collected from the piedmont plain near Manas River (Fig. 2), which features pebbles and sandy gravel deposits. This situation may be explained by (i) binary mixing between post–1989 water and older water recharged between 1950 and 1970 that did not contain CFC–free water (pre–1940) or (ii) mixing of two end–members with one end–member containing various mixtures of young (but pre–1989) and old water and the other end–member having post–1989 water. The second explanation requires samples to contain at least some post–bomb fractions

from the 1960s (revealed by ^{3}H concentrations; Fig. 9) and both post–1989 and pre–1940 water, which is not consistent with CFC data (Fig. 7a). If the first explanation is true, the binary mixing hypothesis and the young water (post–1940) fractions in Table 2 for these three samples should be adjusted accordingly.

Because atmospheric ^{3}H concentrations have been elevated for a long time, old water components can be identified by ^{3}H concentrations that are anomalously low compared with those of CFCs (Plummer et al., 2006b). The G5 sample contained very low CFC–113 with a ^{3}H concentration of 3.8 TU (Table 1), indicating that this sample was likely mixed by the older water (pre–1940) and 1960–1970 water. The low ^{3}H concentration can be attributed to the dilution by a high fraction of old water, and thus the "^{3}H bomb–peak" cannot be recognised. The G16 sample, outside of the shaded region (Fig. 9), has low ^{3}H but a substantial CFC concentration. This situation may be explained by (i) exposure to the atmosphere before sampling during large water table fluctuations due to groundwater pumping or the addition of excess air to water through the fractured system or (ii) river water or reservoir water with high CFC concentration but minimal ^{3}H recharge. Furthermore, the relatively high fractions of young water (89 %; Table 2) preclude the dilution effect by the old water. Irrigation re–infiltration can cause a shift of the CFC concentrations to higher values but does not alter the ^{3}H concentration (Han et al., 2015). However, the relatively low NO_3^- concentrations (4.51 mg L^{-1}; data from Ma et al., 2018) of the G16 sample suggested that irrigation re–infiltration did not have a significant effect. Therefore, river or reservoir water with very low NO_3^- concentration (2.7–7.3 mg L^{-1}; data from Ma et al., 2018) recharge is possible.

4.3 Groundwater mean residence time

4.3.1 ^{3}H and CFCs

RTD functions (Eqs. (3) to (5)) are suited to specific hydrogeological situations (Małoszewski and Zuber, 1982); EPM is particularly useful for interpretation of MRTs in aquifers that have regions of both exponential and piston flow (Cartwright et al., 2017). The unconfined aquifers adjacent to the rivers (Fig. 1 c) are likely to exhibit exponential flow, and recharge through the unsaturated zone (Fig. 1c) will most likely resemble piston flow (Cartwright and Morgenstern, 2015; Cook and Böhlke, 2000). For the time series ^{3}H and CFCs inputs, MRTs (Fig. 10) were initially calculated using EPM, with an EPM ratio of 1.5 obtained using Eqs. (2) and (3) (l_E in Eq. (3) is determined by adding the intermountain depression to the piedmont plain in Fig. 1c). River leakage and rainfall input were possible from the piedmont plain (Ma et al., 2018), thus a less proportion of piston flow by the EPM with an EPM ratio of 2.2 (l_E in Eq. (3) is only in the piedmont plain in Fig. 1c) was also used. To test the veracity the DM with D_P of 0.03 and 0.1 and the EMM were also used to calculate the MRTs via Eqs. (2), (4) and (5). Plots of the output concentrations for ^{3}H (Fig. 10a) and CFCs (CFC–11 in Fig. 10b, CFC–12 in Fig. 10c and CFC–113 in Fig. 10d) vs. MRTs for different lumped parameter models show wide MRTs ranges that increase with the increasing MRTs.

Figure 11 shows that different LPMs yield different MRTs for the same time series of ^{3}H and CFC concentrations. MRTs obtained from different LPMs tend to become more discretized by model with increasing MRTs. For the CFC rainfall inputs,

MRTs from EPM with an EPM ratio of 1.5 (Fig. 11a) varied from 19 to 101 yrs (median: 51 yrs) for the CFC–12 rainfall input, from 33 to 115 yrs (median: 62.3 yrs) for the CFC–11 rainfall input, and from 18 to 92 yrs (median: 50.2 yrs) for the CFC–113 rainfall input. Good linear relationships for MRTs between the different CFC rainfall inputs were obtained using the same EPM (EPM (1.5) in Fig. 11a and EPM (2.2) in Fig. 11b). MRTs increased with decreasing EPM ratios (from 2.2 to 1.5; Fig. 11b), implying that the longer flow paths were recharged from the intermountain depression. For the range of CFC–12 concentrations in the UG and in the west bank of the East Main Canal of MG, similar MRTs were estimated from the different LPMs (Fig. 11b) with mean values varying from 28.6 to 64.8 yrs, whereas those in the east bank (Figs. 2 and 11b and Table 2) of MG show larger differences with mean values varying from 129.2 to 173 yrs. Overall, the youngest value was observed in the G3 sample (south of the fault), and the oldest was in the G5 sample (east bank of the East Main Canal; Fig. 2).

In contrast to the CFC rainfall inputs, MRTs estimated using the ^{3}H rainfall inputs by different LPMs (Fig. 11c) show larger uncertainties and wider ranges. For EPM with an EPM ratio of 1.5, MRTs vary from 19 to 158 yrs with a median of 112.2 yrs (Fig. 11c), which are much longer than those calculated from the CFC rainfall inputs by the same model (Fig. 11b). The differences could be due to the longer travel times through the thick unsaturated zone for ^{3}H than CFCs. ^{3}H moves principally in the liquid phase, whereas CFCs travel in the gas phase through the unsaturated zone (Cook and Solomon, 1995). The more rapid transport for gas–phase than liquid–phase in the unsaturated zone would be expected to give rise to longer residence times from ^{3}H than those determined from CFCs (Cook, et al., 2017). Furthermore, the ranges in MRTs estimated from EPM with EPM ratios of 1.5 and 2.2, DM with D_p of 0.03 and 0.1, and EMM are 16–158 yrs, 72–285 yrs, and 30–360 yrs, respectively. Similar MRT trends were calculated from the CFC–12 input (Fig. 11b), in which the west and east banks of the East Main Canal of MG and DG were separated. Uncertainties increase with increasing MRTs among the different models, especially when MRTs are higher than 130 yrs (Fig. 11c), which mainly occurred in samples collected from the east bank of the East Main Canal of MG and DG.

Because the east bank groundwater had a relatively short distance to mountain and a much smaller hydraulic gradient (Fig. 2), the MRTs were much longer than those in the west bank. That in the west bank shows an overall increasing trend with the distance to mountain in MG and DG (Fig. 11b, c) as the longer and deeper flow paths usually give rise to the longer MRTs (Cartwright and Morgenstern, 2015, 2016; McGuire et al., 2005). Despite the influence from the uncertainties of the input concentrations and different models (Cartwright and Morgenstern, 2015, 2016), MRTs have been identified to vary on account of more complex interplay of factors like mixing and dispersion in the flow systems, which may result in significantly different MRTs from results calculated by LPMs assuming a homogeneous aquifer with a simple geometry to the actual results (Cartwright et al., 2017; Kirchner, 2016; Stewart et al., 2017). Nevertheless, in this study the homogeneous aquifers, being at steady–state, justifying the use of LPMs to calculate MRTs.

4.3.2 Hydrochemistry evolution

Strong correlations between hydrochemical components and groundwater age permit their use as proxies for or complementary to age via previously established relationships in close lithological conditions. For example, an excellent correlation between silica (SiO_2) and MRTs (R^2=0.997) was reported (Morgenstern et al., 2010), which was much higher than in Fig. 12 and in other results (Morgenstern et al., 2015). SiO_2(Fig. 12a), sulfate (SO_4^{2-}), bicarbonate (HCO_3^-), and total dissolved solids (TDS) (Fig. 12b) all show good correlations with groundwater age, indicating that mineral dissolutions through water–rock interactions dominate hydrochemical changes (Ma et al., 2018), and major ion concentrations increase with groundwater age. However, MRTs estimated using ^3H activity showed poor correlations with the ions (data not shown). Moreover, the lithology type groundwater flow through within the aquifer and the likely evolutionary path ways play an important role in the hydrochemical compositions. The negative saturation indices with respect to gypsum of all water (Ma et al., 2018) indicated that the high SO_4^{2-} concentrations (Fig. 12b) were due to the gypsum dissolution in the Tertiary stratum. Also note that high SO_4^{2-} can be originated from the geothermal water (Morgenstern et al., 2015), in contrast to studies such as Guo et al. (2014) and Guo et al. (2017), and can be biased due to anoxic SO_4^{2-} reduction. However, the groundwater with relatively low temperatures and aerobic environment (Table 1) make the two cases above unlikely.

The combination of hydrochemistry concentrations and groundwater age data is also a powerful tool for investigating the groundwater flow processes and flow through conditions (McGuire and McDonnell, 2006; Morgenstern et al., 2010, 2015), identifying the natural groundwater evolution and the impact of anthropogenic contaminants (Morgenstern et al., 2015; Morgenstern and Daughney, 2012). The pH of groundwater decreases from 10.1 to 8.6 over the age range from 19 to 101 yrs, with a log law fit of $\mathrm{pH} = 0.72 \times \ln(\mathrm{MTTs}) + 11.85,\ R^2 = 0.65$ (Fig. 12a). On the contrary, a trend of increasing pH with increasing groundwater age has been reported in New Zealand (the dashed red line shown in Fig. 12a; Morgenstern et al., 2015), where the pH values were overall less than 7.2. These two discrepant trends can be explained by the relationship between the pH and HCO_3^- concentrations in water (inserted plot in Fig. 12a), which the pH increase with increasing HCO_3^- concentrations only when the pH is less than 8.34, otherwise decrease with increasing HCO_3^- concentrations. Therefore, the trend of increasing HCO_3^- concentrations with increasing groundwater age (Fig. 12b) in this study indicates that decreasing trend for the pH (from 10.1 to 8.6) is reasonable.

The soda waters with the overall pH higher than 8.1 (Table 1) are in disequilibrium with primary rock–forming minerals of the host rocks. The incongruent dissolutions of the albite and anorthite through hydrolysis reaction are:

$$2NaAlSi_3O_8 + 11H_2O = Al_2Si_2O_5(OH)_4 + 2Na^+ + 4H_4SiO_4 + 2OH^- \quad \text{(R2)}$$

$$CaAl_2Si_2O_8 + 3H_2O = Al_2Si_2O_5(OH)_4 + Ca^{2+} + 2OH^-, \quad \text{(R3)}$$

where all the chemical components of the albite and anorthite release into the solution phase and produce OH^- with simultaneous precipitation of kaolinite. A trend of increasing pH with well depth (Table 1) suggests that groundwater with pH lower than 9 was likely recharged by CO2–containing water, because OH^- generally interacts with CO2 and organic acids in the soil to form HCO_3^- (Wang et al., 2009). Similarly, the trend of decreasing pH with increasing MRTs (Fig. 12a)

indicates that water containing higher CO_2 concentrations has longer MRT, which seems to suggest the anthropogenic input. The nitrate (NO_3^-) concentrations varied from 4.5 to 20.2 mg L^{-1} with a median of 12.2 mg L^{-1} (data not shown), which exceeded the natural nitrate concentration in groundwater of 5–7 mg L^{-1} (Appelo and Postma, 2005). The development of the plough after the 1950s, N–NO_3 fertiliser (with low $^{87}Sr/^{86}Sr$ ratios; Ma et al., 2018) and the extensive groundwater withdrawal for irrigation (Ji, 2016) suggest that irrigation infiltration could account for the high groundwater NO_3^- concentrations in the piedmont plain. However, little irrigation infiltration was observed in the downstream area with groundwater NO_3^- concentrations of less than 5 mg L^{-1} (Ma et al., 2018) due to the water–saving irrigation style, which did not contribute to groundwater recharge in the arid regions of Northwest China.

5 Conclusions

In this study, we used environmental tracers and hydrochemistry to identify the modern and paleo–meteoric recharge sources, to constrain the different end–members mixing ratios, and study the mixed groundwater MRTs in faulted–hydraulic drop alluvium aquifer systems. The paleo–meteoric recharge in a cooler climate was distinguished from the lateral flow from the higher elevation precipitation in the Manas River downstream area. The relatively modern groundwater with young (post–1940) water fractions of 87–100 % was obtained, indicating a small extent of mixing south of the fault. The short MRTs (19 yrs) along with the higher–than–natural NO_3^- concentration (7.86 mg L^{-1}) south of the fault (headwater area) indicated the invasion of modern contaminants. This finding warrants particular attention. High mixing rate amplitudes varying from 12 to 91 % were widespread in north of the fault due to the varying depths of long–screened boreholes as well as within the aquifer itself. Furthermore, the mixing diversity was highlighted by the substantial water table fluctuations during groundwater pumping, vertical recharge through the thick unsaturated zone, and young water mixtures in different decades. The strong correlations between groundwater MRTs and hydrochemical concentrations enable a first–order proxy at different times to be used. In addition, this study has revealed that MRTs estimated by CFCs were more appropriate than those using ^3H in the arid MRB with a thick unsaturated zone.

Author contributions. Xing Liang and Jing Li were responsible for the ^3H and ^{14}C analyses. Bin Ma undertook the sampling program and oversaw the analysis of the hydrochemistry and CFCs. Bin Ma and Menggui Jin prepared the manuscript.

Competing interests. The authors declare that they have no conflict of interest.

Acknowledgements. This research was financially supported by the National Natural Science Foundation of China (no. U1403282 and no. 41807204). The authors would like to thank Dr. Yunquan Wang for the valuable discussions and

suggestions for this paper. We wish to thank Dr. Xumei Mao, Dr. Dajun Qin and Mr. Yalei Liu for sampling and laboratory works. We also wish to thank the editor and anonymous referees for their valuable suggestions and insightful comments.

References

Aggarwal, P. K.: Introduction, in: Isotope Methods for Dating Old Groundwater, Suckow, A., Aggarwal, P. K., and Araguas-Araguas, L. (Eds.), International Atomic Energy Agency, Vienna, Austria, 1–4, 2013.

Appelo, C. A. J. and Postma, D.: Geochemistry, groundwater and pollution, 2nd ed., Balkema, Dordrecht, Netherlands, 2005.

Atkinson, A. P., Cartwright, I., Gilfedder, B. S., Cendón, D. I., Unland, N. P., and Hofmann, H.: Using ^{14}C and ^{3}H to understand groundwater flow and recharge in an aquifer window, Hydrol. Earth Syst. Sci., 18, 4951–4964, doi:10.5194/hess-18-4951-2014, 2014.

Barletta, B., Meinardi, S., Simpson, I. J., Rowland, F. S., Chan, C. Y., Wang, X., Zou, S., Chan, L. Y., and Blake, D. R.: Ambient halocarbon mixing ratios in 45 Chinese cities, Atmos. Environ., 40, 7706–7719, doi:10.1016/j.atmosenv.2006.08.039, 2006.

Batlle–Aguilar, J., Banks, E. W., Batelaan, O., Kipfer, R., Brennwald, M. S., and Cook, P. G.: Groundwater residence time and aquifer recharge in multilayered, semi–confined and faulted aquifer systems using environmental tracers, J. Hydrol., 546, 150–165, doi:10.1016/j.jhydrol.2016.12.036, 2017.

Benettin, P., Volkmann, T. H. M., Freyberg, J., Frentress, J., Penna, D., Dawson, T. E., and Kirchner, J. W.: Effects of climatic seasonality on the isotopic composition of evaporating soil waters, Hydrol. Earth Syst. Sci., 22, 2881–2890, doi:10.5194/hess–22–2881–2018, 2018.

Beyer, M., Jackson, B., Daughney, C., Morgenstern, U., and Norton, K.: Use of hydrochemistry as a standalone and complementary groundwater age tracer, J. Hydrol., 543, 127–144, doi:10.1016/j.jhydrol.2016.05.062, 2016.

Carlson, M. A., Lohse, K. A., McIntosh J. C., and McLain J. E. T.: Impacts of urbanization on groundwater quality and recharge in a semi–arid alluvial basin, J. Hydrol., 409, 196–211, doi:10.1016/j.jhydrol.2011.08.020, 2011.

Cartwright, I., Cendón, D., Currell, M., and Meredith, K.: A review of radioactive isotopes and other residence time tracers in understanding groundwater recharge: Possibilities, challenges, and limitations, J. Hydrol., 555, 797–811, doi:10.1016/j.jhydrol.2017.10.053, 2017.

Cartwright, I., Irvine, D., Burton, C., and Morgenstern, U.: Assessing the controls and uncertainties on mean transit times in contrasting headwater catchments, J. Hydrol., 557, 16–29, doi:10.1016/j.jhydrol.2017.12.007, 2018.

Cartwright, I. and Morgenstern, U.: Contrasting transit times of water from peatlands and eucalypt forests in the Australian Alps determined by tritium: implications for vulnerability and source of water in upland catchments, Hydrol. Earth Syst. Sci., 20, 4757–4773, doi:10.5194/hess-20-4757-2016, 2016.

Cartwright, I. and Morgenstern, U.: Transit times from rainfall to baseflow in headwater catchments estimated using tritium: the Ovens River, Australia, Hydrol. Earth Syst. Sci., 19, 3771–3785, doi:10.5194/hess-19-3771-2015, 2015.

Chen, Z., Qi, J., Xu, J., X, J., Ye, H., and Nan, Y.: Paleoclimatic interpretation of the past 30 ka from isotopic studies of the deep confined aquifer of the North China Plain, Appl. Geochem., 18, 997–1009, doi:10.1016/S0883-2927(02)00206-8, 2003.

Clark, I. D. and Fritz. P.: Environmental Isotopes in Hydrogeology, Lewis, New York, USA, 1997.

Craig, H.: Isotopic variations in meteoric waters, Science, 133, 1702–1703, doi:10.1126/science.133.3465.1702, 1961.

Cook, P. G., and Böhlke, J. K.: Determining timescales for groundwater flow and solute transport, in: Environmental Tracers in Subsurface Hydrology, Cook, P. G. and Herczeg, A. L. (Eds.), Kluwer, Boston, Netherlands, 1–30, 2000.

Cook, P., Dogramaci, S., McCallum, J., and Hedley, J.: Groundwater age, mixing and flow rates in the vicinity of large open pit mines, Pilbara region, northwestern Australia, Hydrogeol. J., 25, 39–53, doi:10.1007/s10040-016-1467-y, 2017.

Cook, P. G., Plummer, L. N., Solomon, D. K., Busenberg, E., and Han, L. F.: Effects and processes that can modify apparent CFC age, in: Use of Chlorofluorocarbons in Hydrology: A Guidebook, Gröning, M., Han, L. F., and Aggarwal, P. (Eds.), International Atomic Energy Agency, Vienna, Austria, 31–58, 2006.

Cook, P. G. and Solomon, D. K.: Transport of atmospheric tracer gases to the water table: Implications for groundwater dating with chlorofluorocarbons and krypton 85, Water Resour. Res., 31, 263–270, doi:10.1029/94WR02232, 1995.

Cui, W. G., Mu, G. J., Wen, Q., and Yue, J.: Evolution of alluvial fans and reaction to the regional activity at rage front of Manas River Valley, Res. Soil Water Conserv., 14, 161–163, 2007.

Custodio, E., Jódar, J., Herrera, C., Custodio-Ayala, J., and Medina, A.: Changes in groundwater reserves and radiocarbon and chloride content due to a wet period intercalated in an arid climate sequence in a large unconfined aquifer, J. Hydrol., 556, 427–437, doi:10.1016/j.jhydrol.2017.11.035, 2018.

Dansgaard, W.: Stable isotopes in precipitation, Tellus, 16, 436–468, doi:10.1111/j.2153-3490.1964.tb00181.x, 1964.

Darling, W. G., Gooddy, D. C., MacDonald, A. M., and Morris, B. L.: The practicalities of using CFCs and SF_6 for groundwater dating and tracing, Appl. Geochem., 27, 1688–1697, doi:10.1016/j.apgeochem.2012.02.005, 2012.

Dawson, T. E. and Ehleringer, J. R.: Streamside trees do not use stream water, Nature, 350, 335–337, 1991.

Dreuzy, J. R. D. and Ginn, T. R.: Residence times in subsurface hydrological systems, introduction to the Special Issue, J. Hydrol., 543, 1–6, doi:10.1016/j.jhydrol.2016.11.046, 2016.

Edmunds, W. M., Ma, J., Aeschbach–Hertig, W., Kipfer, R., and Darbyshire, D. P. F.: Groundwater recharge history and hydrogeochemical evolution in the Minqin Basin, North West China, Appl. Geochem., 21, 2148–2170, doi:10.1016/j.apgeochem.2006.07.016, 2006.

Gleeson, T., Befus, K. M., Jasechko, S., Luijendijk, E., and Cardenas, M. B.: The global volume and distribution of modern groundwater, Nat. Geosci., 9, 161–167, doi:10.1038/NGEO2590, 2016.

Guo, H., Wen, D., Liu, Z., Jia, Y., and Guo, Q.: A review of high arsenic groundwater in Mainland and Taiwan, China: Distribution, characteristics and geochemical processes, Appl. Geochem., 41, 196–217, doi:10.1016/j.apgeochem.2013.12.016, 2014.

Guo, Q., Planer–Friedrich, B., Liu, M., Li, J., Zhou, C., and Wang, Y.: Arsenic and thioarsenic species in the hot springs of the Rehai magmatic geothermal system, Tengchong volcanic region, China, Chem. Geol., 453, 12–20, doi:10.1016/j.chemgeo.2017.02.010, 2017.

Green, C. T., Jurgens, B. C., Zhang, Y., Starn, J. J., Singleton, M. J., and Esser, B. K.: Regional oxygen reduction and denitrification rates in groundwater from multi–model residence time distributions, San Joaquin Valley, USA, J. Hydrol., 543, 155–166, doi:10.1016/j.jhydrol.2016.05.018, 2016.

Han, D., Cao, G., McCallum, J., and Song, X.: Residence times of groundwater and nitrate transport in coastal aquifer systems: Daweijia area, northeastern China, Sci. Total Environ., 538, 539–554, doi:10.1016/j.scitotenv.2015.08.036, 2015.

Han, D., Song, X., Currell, M. J., Cao, G., Zhang, Y., and Kang, Y.: A survey of groundwater levels and hydrogeochemistry in irrigated fields in the Karamay Agricultural Development Area, northwest China: Implications for soil and groundwater salinity resulting from surface water transfer for irrigation, J. Hydrol., 405, 217–234, doi:10.1016/j.jhydrol.2011.03.052, 2011.

Han, D. M., Song, X. F., Currell, M. J., and Tsujimura, M.: Using chlorofluorocarbons (CFCs) and tritium to improve conceptual model of groundwater flow in the South Coast Aquifers of Laizhou Bay, China, Hydrol. Process., 26, 3614–3629, doi:10.1002/hyp.8450, 2012.

Han, L., Hacker, P., and Gröning, M.: Residence times and age distributions of spring waters at the Semmering catchment area, Eastern Austria, as inferred from tritium, CFCs and stable isotopes, Isot. Environ. Healt. S., 43, 31–50, doi:10.1080/10256010601154015, 2007.

Horneman, A., Stute, M., Schlosser, P., Smethie Jr. W., Santella, N., Ho, D. T., Mailloux, B., Gorman, E., Zheng, Y., and van Geen, A.: Degradation rates of CFC–11, CFC–12 and CFC–113 in anoxic shallow aquifers of Araihazar Bangladesh, J. Contam. Hydrol., 97, 27–41, doi:10.1016/j.jconhyd.2007.12.001, 2008.

Hrachowitz, M., Soulsby, C., Tetzlaff, D., Dawson, J. J. C., Dunn, S. M., and Malcolm, I. A.: Using long–term data sets to understand transit times in contrasting headwater catchments, J. Hydrol., 367, 237–248, doi:10.1016/j.jhydrol.2009.01.001, 2009.

Huang, T., Pang, Z., Li, J., Xiang, Y., and Zhao, Z.: Mapping groundwater renewability using age data in the Baiyang alluvial fan, NW China, Hydrogeol. J., 25, 743–755, doi:10.1007/s10040-017-1534-z, 2017.

IAEA: http://isohis.iaea.org/water, last access: 27 January 2016, 2006.

Jelinowska, A., Tucholka, P., Gasse, F., and Fontes, J. C.: Mineral magnetic record of environment in Late Pleistocene and Holocene sediments, Lake Manas, Xinjiang, China, Geophys. Res. Lett., 22, 953–956, doi:10.1029/95GL00708, 1995.

Ji, L.: Using stable hydrogen and oxygen isotope to research the conversion relationship of surface water and groundwater in Manas River Basin, M.S. thesis, Shihezi University, China, 58 pp., 2016.

Jurgens, B. C., Böhlke, J. K., and Eberts, S. M.: TracerLPM (Version 1): An Excel® workbook for interpreting groundwater age distributions from environmental tracer data: U.S. Geological Survey Techniques and Methods Report 4–F3, Reston, USA, 60 pp., 2012.

Kirchner, J. W.: Aggregation in environmental systems – Part 1: Seasonal tracer cycles quantify young water fractions, but not mean transit times, in spatially heterogeneous catchments, Hydrol. Earth Syst. Sci., 20, 279–297, doi:10.5194/hess-20-279-2016, 2016.

Kirchner, J. W., Tetzlaff, D., and Soulsby C.: Comparing chloride and water isotopes as hydrological tracers in two Scottish catchments, Hydrol. Process., 24, 1631–1645, doi:10.1002/hyp.7676, 2010.

Koh, D. C., Ha, K., Lee, K. S., Yoon, Y. Y., and Ko, K. S.: Flow paths and mixing properties of groundwater using hydrogeochemistry and environmental tracers in the southwestern area of Jeju volcanic island, J. Hydrol., 432–433, 61–74, doi:10.1016/j.jhydrol.2012.02.030, 2012.

Kong, Y. and Pang, Z.: A positive altitude gradient of isotopes in the precipitation over the Tianshan Mountains: Effects of moisture recycling and sub–cloud evaporation, J. Hydrol., 542, 222–230, doi:10/1016/j.jhydrol.2016.09.007, 2016.

Li, J., Pang, Z., Froehlich, K., Huang, T., Kong, Y., Song, W., and Yun, H.: Paleo–environment from isotopes and hydrochemistry of groundwater in East Junggar Basin, Northwest China, J. Hydrol., 529, 650–661, doi:10.1016/j.jhydrol.2015.02.019, 2015.

Ma, B., Jin, M., Liang, X., and Li, J.: Groundwater mixing and mineralization processes in a mountain–oasis–desert basin, northwest China: hydrogeochemistry and environmental tracer indicators, Hydrogeol. J., 26, 233–250, doi:10.1007/s10040-017-1659-0, 2018.

Ma, B., Liang, X., Jin, M., Li, J., and Niu, H.: Characteristics of fractionation of hydrogen and oxygen isotopes in evaporating water in the typical region of the North China Plain, Adv. Water Sci., 26, 639–648, doi:10.14042.j.cnki.32.1309.2015.05.005, 2015.

Mahlknecht, J., Hernández–Antonio, A., Eastoe, C. J., Tamez–Meléndez, C., Ledesma–Ruiz, R., Ramos–Leal, J. A., and Ornelas–Soto, N.: Understanding the dynamics and contamination of an urban aquifer system using groundwater age (^{14}C, ^{3}H, CFCs) and chemistry, Hydrol. Process., 31, 2365–2380, doi:10.1002/hyp.11182, 2017.

Małoszewski, P.: Lumped–parameter models as a tool for determining the hydrological parameters of some groundwater systems based on isotope data, IAHS–AISH Publication, 271–276, 2000.

Małoszewski, P. and Zuber, A.: Determining the turnover time of groundwater systems with the aid of environmental tracers, 1. Models and their applicability, J. Hydrol., 57, 207–231, doi:10.1016/0022-1694(82)90147-0, 1982.

McGuire, K. J. and McDonnell, J. J.: A review and evaluation of catchment transit time modeling, J. Hydrol., 330, 543–563, doi:10.1016/j.jhydrol.2006.04.020, 2006.

McGuire, K. J., McDonnell, J. J., Weiler, M., Kendall, C., McGlynn, B. L., Welker, J. M., and Seibert, J.: The role of topography on catchment–scale water residence time, Water Resour. Res., 41, 302–317, doi:10.1029/2004WR003657, 2005.

Morgenstern, U. and Daughney, C. J.: Groundwater age for identification of baseline groundwater quality and impacts of land–use intensification – The National Groundwater Monitoring Programme of New Zealand, J. Hydrol., 456–457, 79–93, doi:10.1016/j.jhydrol.2012.06.010, 2012.

Morgenstern, U., Daughney, C. J., Leonard, G., Gordon, D., Donath, F. M., and Reeves, R.: Using groundwater age and hydrochemistry to understand sources and dynamics of nutrient contamination through the catchment into Lake Rotorua, New Zealand, Hydrol. Earth Syst. Sci., 19, 803–822, doi:10.5194/hess-19-803-2015, 2015.

Morgenstern, U., Stewart, M. K., and Stenger, R: Dating of streamwater using tritium in a post nuclear bomb pulse world: continuous variation of mean transit time with streamflow, Hydrol. Earth Syst. Sci., 14, 2289–2301, doi:10.5194/hess-14-2289-2010, 2010.

Morgenstern, U. and Taylor, C. B.: Ultra low–level tritium measurement using electrolytic enrichment and LSC, Isot. Environ. Healt. S., 45, 96–117, doi:10.1080/10256010902931194, 2009.

Négrel, P., Petelet–Giraud, E., and Millot, R.: Tracing water cycle in regulated basin using stable δ^2H–$\delta^{18}O$ isotopes: The Ebro river basin (Spain), Chem. Geol., 422, 71–81, doi:10.1016/j.chemgeo.2015.12.009, 2016.

Oster, H., Sonntag, C., and Münnich, K. O.: Groundwater age dating with chlorofluorocarbons, Water Resour. Res., 32, 1989–3001, doi:10.1029/96WR01775, 1996.

Pearson, F. J. and Hanshaw, B. B.: Sources of dissolved carbonate species in groundwater and their effects on carbon–14 dating, in: Proceedings of A Symposium on Use of Isotopes in Hydrology, International Atomic Energy Agency, Vienna, Austria, 271–286, 1970.

Plummer, L. N., Busenberg, E., and Cook, P. G.: Principles of Chlorofluorocarbon dating, in: Use of Chlorofluorocarbons in Hydrology: A Guidebook, Gröning, M., Han, L. F., and Aggarwal, P. (Eds.), International Atomic Energy Agency, Vienna, Austria, 17–29, 2006a.

Plummer, L. N., Busenberg, E., and Han, L. F.: CFCs in binary mixtures of young and old groundwater, in: Use of Chlorofluorocarbons in Hydrology: A Guidebook, Gröning, M., Han, L. F., and Aggarwal, P. (Eds.), International Atomic Energy Agency, Vienna, Austria, 59–72, 2006b.

Polach, H. A.: Evaluation and status of liquid scintillation counting for radiocarbon dating, Radiocarbon, 29, 1–11, doi:10.1017/S0033822200043502, 1987.

Qin, D.: Decline in the concentrations of chlorofluorocarbons (CFC–11, CFC–12 and CFC–113) in an urban area of Beijing, China, Atmos. Environ., 41, 8424–8430, doi:10.1016/j.atmosenv.2007.07.005, 2007.

Qin, D., Qian, Y., Han, L., Wang, Z., Li, C., and Zhao, Z.: Assessing impact of irrigation water on groundwater recharge and quality in arid environment using CFCs, tritium and stable isotopes, in the Zhangye Basin, Northwest China, J. Hydrol., 405, 194–208, doi:10.1016/j.jhydrol.2011.05.023, 2011.

Russell, A. D. and Thompson, G. M.: Mechanisms leading to enrichment of the atmospheric fluorocarbons CCl_3F and CCl_2F_2 in groundwater, Water Resour. Res., 19, 57–60, doi:10.1029/WR019i001p00057, 1983.

Stewart, M. K., Morgenstern, U., Gusyev, M. A., and Małoszewski, P.: Aggregation effects on tritium–based mean transit times and young water fractions in spatially heterogeneous catchments and groundwater systems, Hydrol. Earth Syst. Sci., 21, 4615–4627, doi:10.5194/hess-21-4615-2017, 2017.

Stewart, M. K., Morgenstern, U., and McDonnell, J. J.: Truncation of stream residence time: how the use of stable isotopes has skewed our concept of stream water age and origin, Hydrol. Process., 24, 1646–1659, doi:10.1002/hyp.7576, 2010.

Suckow, A.: The age of groundwater – Definitions, models and why we do not need this term, App. Geochem, 50, 222–230, doi:10.1016/j.apgeochem.2014.04.016, 2014.

Tadros, C. V., Hughes, C. E., Crawford, J., Hollins, S. E., and Chisari, R.: Tritium in Australian precipitation: A 50 year record, J. Hydrol., 513, 262–273, doi:10.1016/j.jhydrol.2014.03.031, 2014.

Visser, A., Broers, H. P., Purtschert, R., Sültenfuß, J., and de Jonge, M.: Groundwater age distributions at a public drinking water supply well field derived from multiple age tracers (^{85}Kr, ^{3}H/^{3}He, and ^{39}Ar), Water Resour. Res., 49, 7778–7796, doi:10.1002/2013WR014012, 2013.

Vogel, J. C.: Carbon–14 dating of groundwater, in: Proceedings of A Symposium on Use of Isotopes in Hydrology, International Atomic Energy Agency, Vienna, Austria, 225–239, 1970.

Wang, Y., Shvartsev, S. L., and Su, C.: Genesis of arsenic/fluoride–enriched soda water: A case study at Datong, northern China, Appl. Geochem., 24, 641–649, doi:10.1016/j.apgeochem.2008.12.015, 2009.

Wu, B.: Study on groundwater system evolvement law and water environment effect of Shihezi City, Ph.D. thesis, Xinjiang Agricultural University, China, 132 pp., 2007.

Zhao, B. F.: Recharge on water resources characteristics and its rational development pattern for arid areas: a case of Manas River Basin, Ph.D. thesis, Chang'an University, China, 182 pp., 2010.

Zhou, H. C.: Groundwater system and recharge from the remote river in Southwestern margin of the Jungger Basin, Ph.D. thesis, Chinese Academy of Geological Sciences, China, 116 pp., 1992.

Table 1. Chemical–physical parameters, stable isotopes, tritium (^{3}H), ^{14}C, and CFC concentrations in groundwater samples in the Manas River Basin.

Sample ID	Sampling date (d/m/y)	Elevation (m a.s.l.)[a]	Well depth (m)	pH	T (℃)	EC (μS cm^{-1})	DO (mg L^{-1})	$\delta^{2}H$ (‰)	$\delta^{18}O$ (‰)	CFC–11 (pmol L^{-1})	CFC–12 (pmol L^{-1})	CFC–113 (pmol L^{-1})	^{3}H (TU)	$a^{14}C$ (pMC)	$^{14}C_{corr}$ age (years)
Upstream groundwater (UG)															
G1	5/6/2015	1083	170[b]					–67.60	–10.15				41.07		
G2	5/6/2015	1107	170[b]					–67.40	–10.17				41.13		
G3	9/8/2015	755	150	10.1	11.5	387	9.8	–70.39	–10.50	3.14	2.18	0.38			
G4	6/6/2015	532	58					–66.80	–9.91				60.04		
Midstream groundwater (MG)															
G5	8/8/2015	467	100	8.6	13.4	896	4.6	–69.35	–10.73	0.17	0.19	0.02	3.80		
G6	8/6/2015	472	175										28.90		
G7	7/8/2015	422	100	8.8	15.7	620	3.7	–69.87	–10.98	0.27	0.27	0.03			
G8	7/8/2015	412	90	9.3	13.6	513	2.1	–69.92	–11.08	1.99	1.21	0.18	5.00		
G9	8/8/2015	484	100	9.1	14.5	612	9.1	–74.58	–11.01	1.31	1.03	0.13	7.10		
G10	8/6/2015	463	145					–72.30	–11.05				9.09		
G11	8/6/2015	439	60					–68.50	–10.47				15.75		
G12	7/8/2015	368	260	9.3	19.0	327	6.7	–69.33	–10.73					86.9	−684
G13	4/8/2015	370	300	9.4	17.1	307	1.2	–76.20	–11.22					54.6	3158
G14	4/8/2015	370	60	9.0	13.2	556	1.4	–68.96	–10.43				1.10		
G15	5/8/2015	364	23	8.1	12.7	1650	1.0	–69.45	–9.86	0.99	0.91	0.14	7.10		
G16	5/8/2015	357	56	9.0	15.2	291	0.7	–76.59	–11.57	2.69	1.54	0.22	4.80		
G17	5/8/2015	367	280	9.8	17.2	263	2.5	–82.45	–12.19					53.2	3373
G18	6/8/2015	377	350[b]	9.0	15.3	233	6.6	–75.97	–11.50					46.8	4432
G19	6/8/2015	381	118[b]	9.0	15.4	309	5.2	–76.46	–11.46				6.90		
G20	6/8/2015	381	13	8.7	12.6	615	2.1	–74.99	–11.27	1.68	1.14	0.16	8.20		

Sample ID	Sampling date (d/m/y)	Elevation (m a.s.l.)[a]	Well depth (m)	pH	T (℃)	EC (μS cm^{-1})	DO (mg L^{-1})	$\delta^{2}H$ (‰)	$\delta^{18}O$ (‰)	CFC–11 (pmol L^{-1})	CFC–12 (pmol L^{-1})	CFC–113 (pmol L^{-1})	^{3}H (TU)	$a^{14}C$ (pMC)	$^{14}C_{corr}$ age (years)
G21	5/8/2015	424	180	8.8	15.6	378	8.0	–77.30	–11.60					43.4	5056
G22	6/6/2015	428	150					–69.72	–10.41				26.29		
G23	6/6/2015	446	70					–67.63	–9.92				37.50		
G24	8/8/2015	453	110	9.1	14.7	571	8.6	–77.35	–11.23	1.53	C[c]	C			
G25	8/8/2015	457	48	9.5	13.6	512	9.8	–77.91	–11.36	2.93	1.67	0.24			
Downstream groundwater (DG)															
G26	10/6/2015	348	40					–85.19	−12.11				6.91		
G27	29/7/2015	323	280	9.0	18.3	244		–79.83	–12.21					23.5	10127
G28	3/8/2015	353	45	9.0	13.2	246	8.0	–78.02	–11.47				2.90		
G29	11/6/2015	347	380					–86.39	−12.33				3.64	34.3	7001

[a] m a.s.l. = m above sea level. [b] Artesian well. [c] Contamination.

Table 2. Calculated results for CFC atmospheric partial pressures (pptv), modern precipitation recharge year, fraction of post−1940 water, and mean residence times (DM, EPM, EMM).

Sample ID	Atmospheric partial pressures (pptv)			Mixing post−1940 water in decimal year (F12/F113)	Fraction of post−1940 water (BM[a], %)	modern precipitation recharge year (calendar year)			Mean residence times (F12) (years)[b]				
	CFC–11	CFC–12	CFC–113			CFC–11	CFC–12	CFC–113	EPM (1.5)	EPM (2.2)	DM (0.03)	DM (0.1)	EMM
G3	179.59	476.18	70.88	1990 2003	100 87	1982	1990	1990	19	22	39	47	16
G5	10.42	43.99	4.04	1983	12	1960	1962	1968	101	73	91	160	440
G7	18.49	68.99	6.85	1985	18	1963	1965	1971	89	66	82	139	270
G8	122.11	280.24	36.42	1988	64	1976	1978	1984	43	39	52	71	49
G9	85.03	251.10	27.96	1985	66	1973	1977	1982	47	42	54	76	58
G15	58.15	202.68	26.99	1988	45	1970	1974	1981	55	47	59	86	77
G16	177.81	380.91	48.36	1987	89	1982	1985	1986	30	31	45	57	29
G20	100.11	257.11	31.36	1987	62	1974	1977	1983	45	41	54	75	56
G24	99.90					1974							
G25	180.79	388.92	48.83	1985	91	1982	1986	1986	30	30	44	56	28

[a] BM=binary mixing, assuming a mixture of old water with young water (post–1940). [b] Lumped parameter models: DM=dispersion model with D_p (in Eq. (3)) of 0.1 and 0.03, EPM=exponential–piston flow model with η (in Eq. (2)) of 2.2 and 1.5, EMM=exponential mixing model. F12 is short for CFC–12.

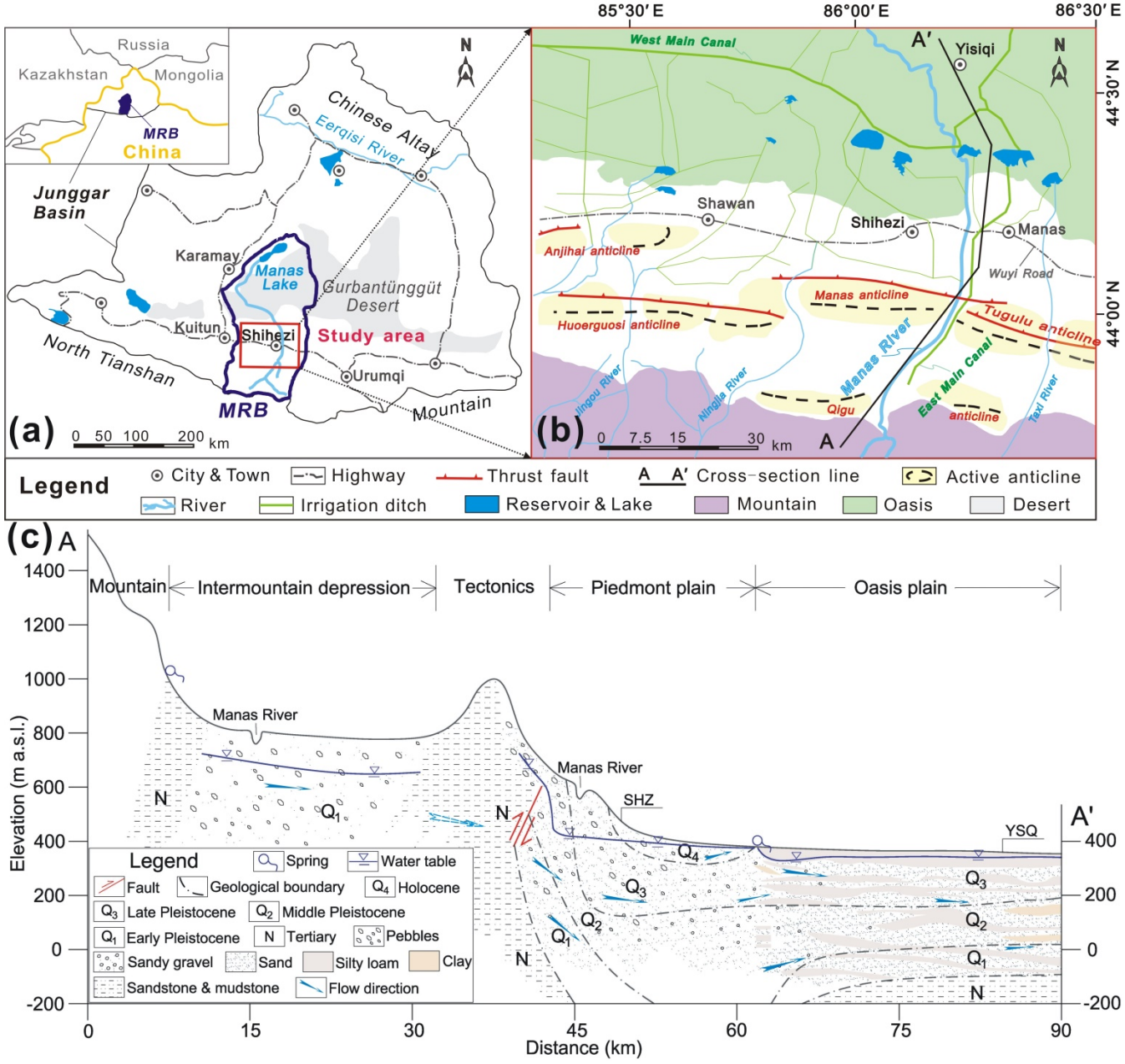

Figure 1. Maps showing (**a**) regional location of the Manas River Basin (modified after Ma et al., 2018), (**b**) surface water (river, reservoir and irrigation ditch) system (modified after Cui et al, (2007) and Ji, (2016)) and (**c**) geological cross–section of the study area for A–A′ line shown in (**b**).

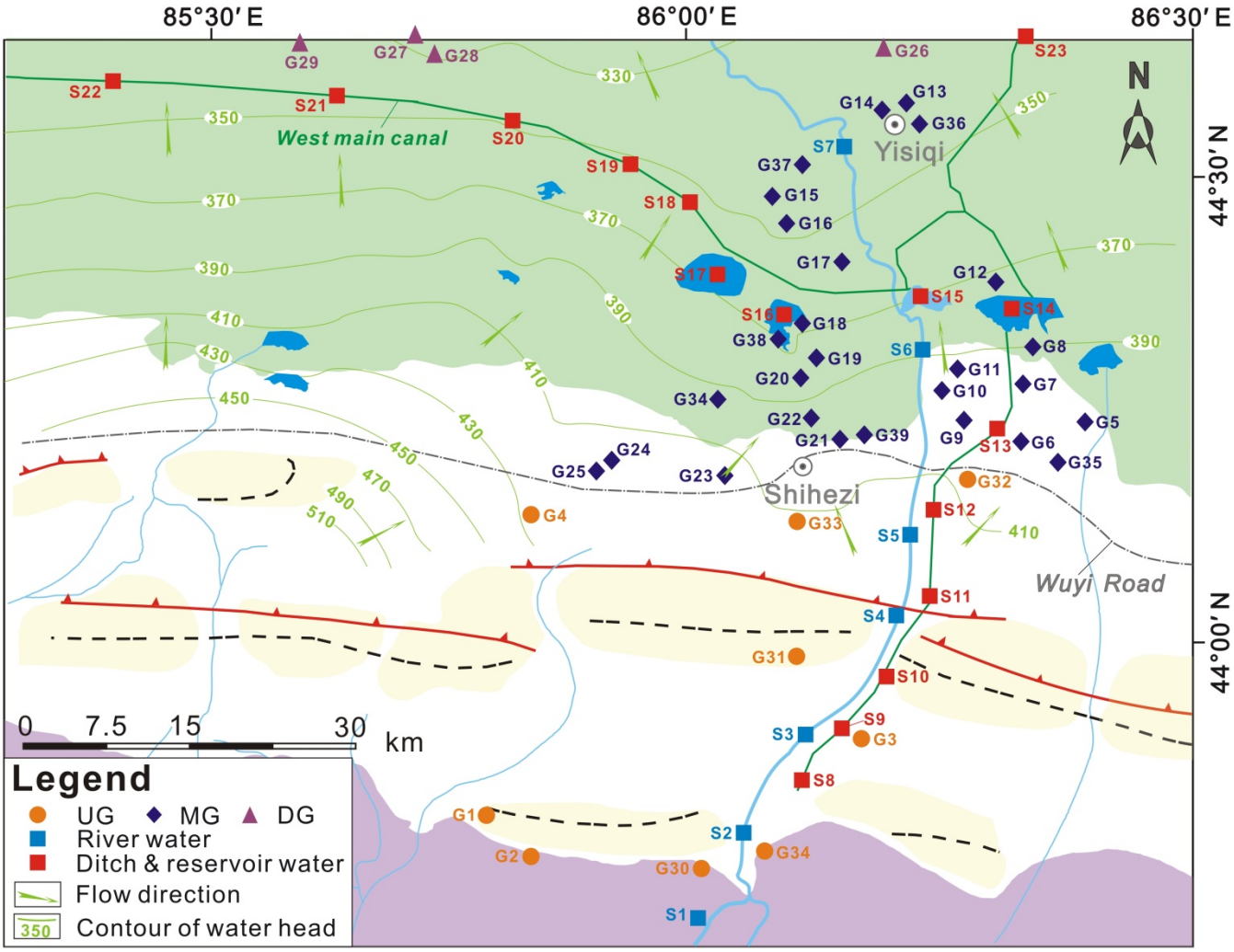

Figure 2. Water sampling sites and unconfined groundwater head contours (in meters) in the headwater catchments of Manas River. UG=Upstream Groundwater, MG=Midstream Groundwater, DG=Downstream Groundwater.

760

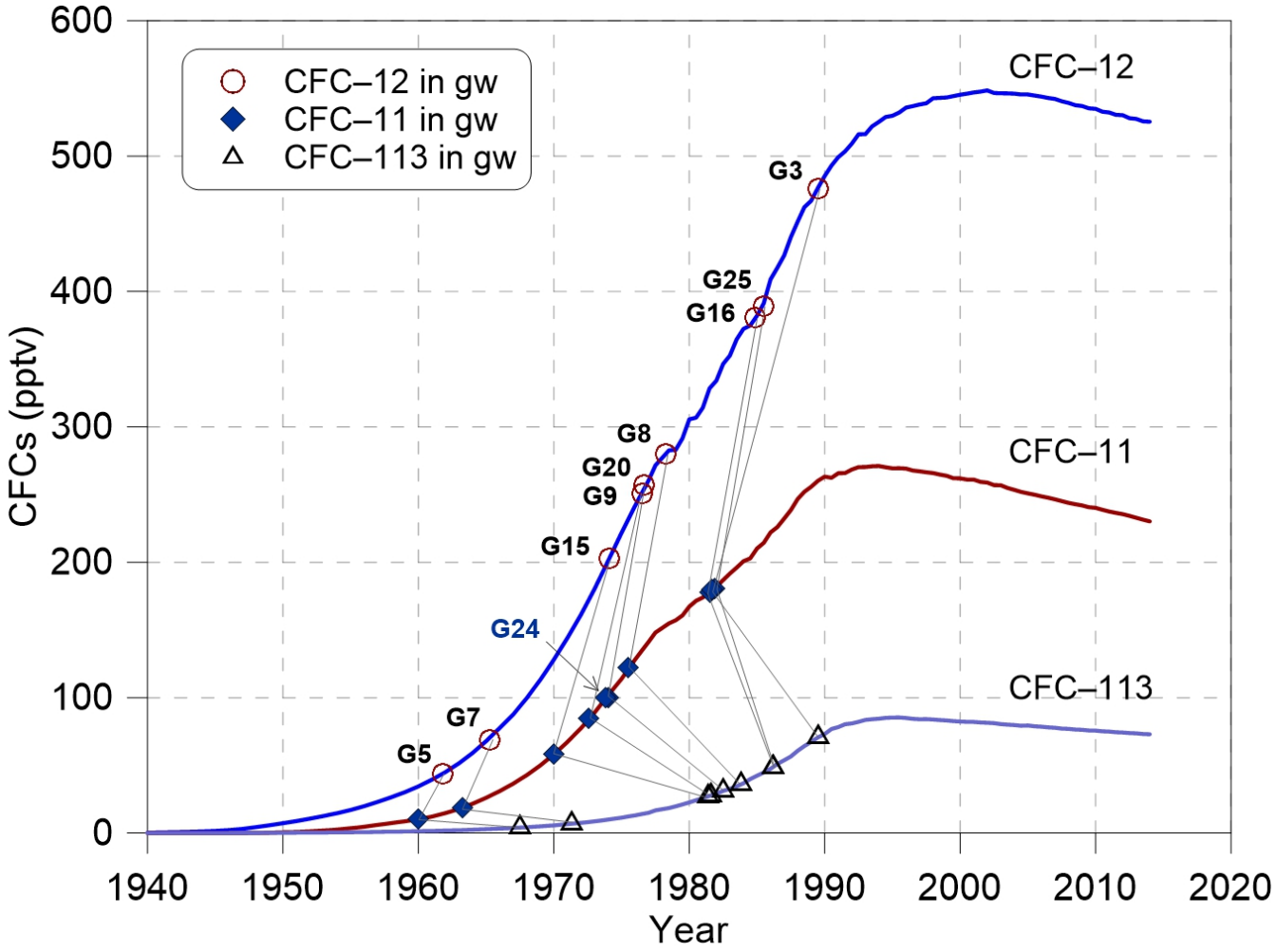

Figure 3. Concentrations of CFC–11, CFC–12 and CFC–113 (pptv) in the groundwater of this study area sampled in 2015 compared with the time series trend of Northern Hemisphere atmospheric mixing ratio at a recharge temperature of 10 ºC. Data is available at < http://water.usgs.gov/lab/software/air/cure/>.

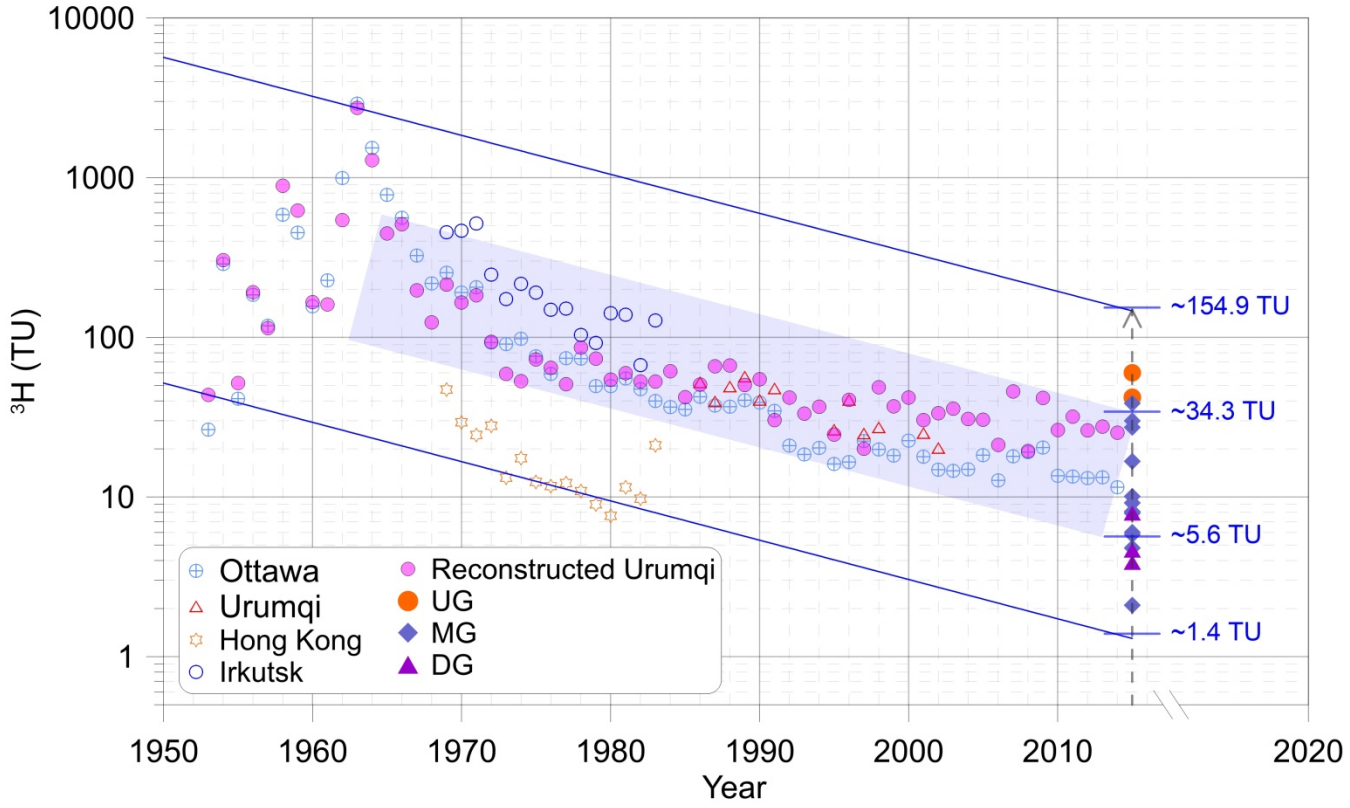

Figure 4. Tritium concentration (TU) of the upstream groundwater (UG), midstream groundwater (MG), and downstream groundwater (DG). Time series of tritium concentration in precipitation at Ottawa, Urumqi, Hong Kong, and Irkutsk were obtained by GNIP in IAEA (https://www.iaea.org/). The blue solid lines and shaded field were drawn using the half–life (12.32 yrs) of tritium decayed to 2014.

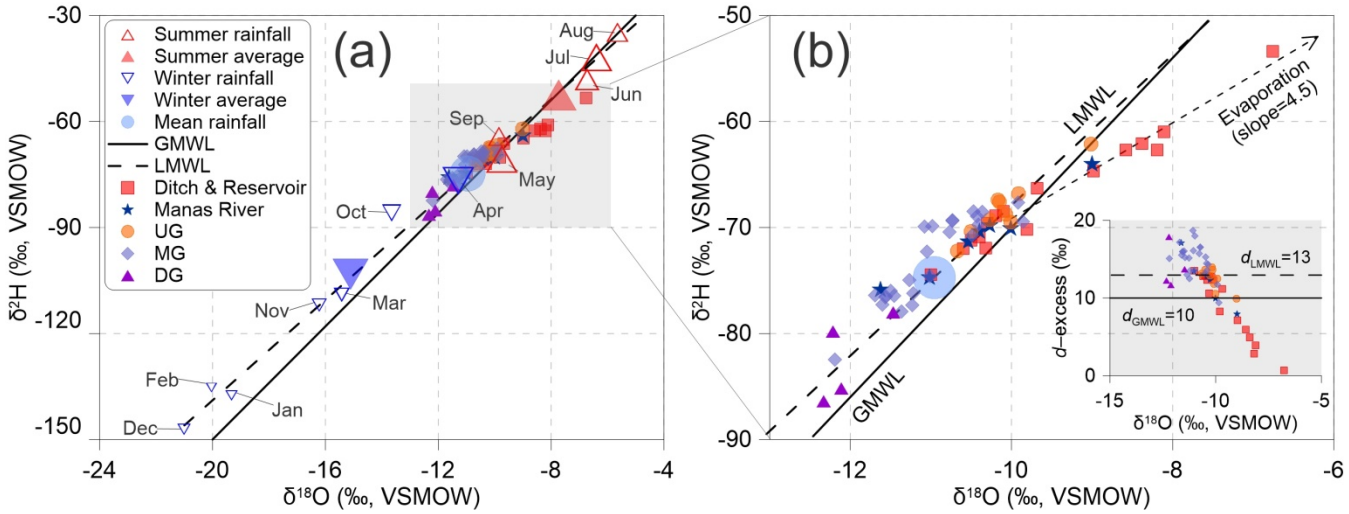

Figure 5. (**a**) Plot of stable isotopes of surface water and groundwater from the mountain to the oasis plain as compared to the global meteoric water line (GMWL; Craig, 1961) and the local meteoric water line (LMWL, rainfall in Urumqi station of IAEA networks during 1986 and 2003; IAEA, 2006). The size of the hollow triangles stands for the relative amount of precipitation. "Mean rainfall" refers to the annual amount–weighted mean rainfall isotopic value. (**b**) Plot of δ^2H vs. $\delta^{18}O$ and inserted plot *d*–excess vs. $\delta^{18}O$. UG=Upstream Groundwater, MG=Midstream Groundwater, DG=Downstream Groundwater.

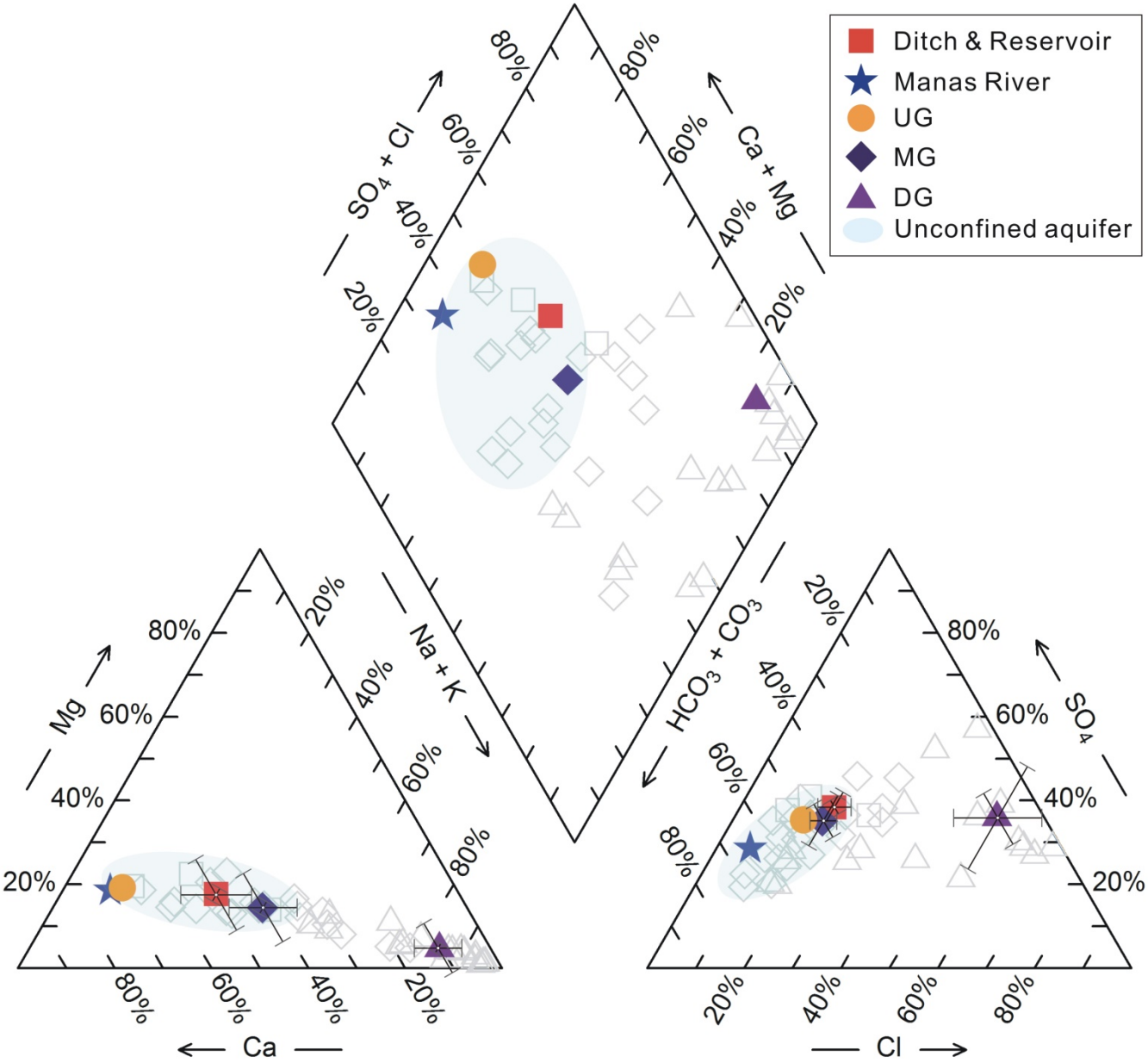

785 **Figure 6.** Piper diagram highlights the HCO_3–SO_4–Na type of waters. The coloured symbols represent the mean values calculated from the hydrochemistry data (light grey hollow symbols) reported by Ma et al. (2018). The error bars are shown in the cation and anion diagrams.

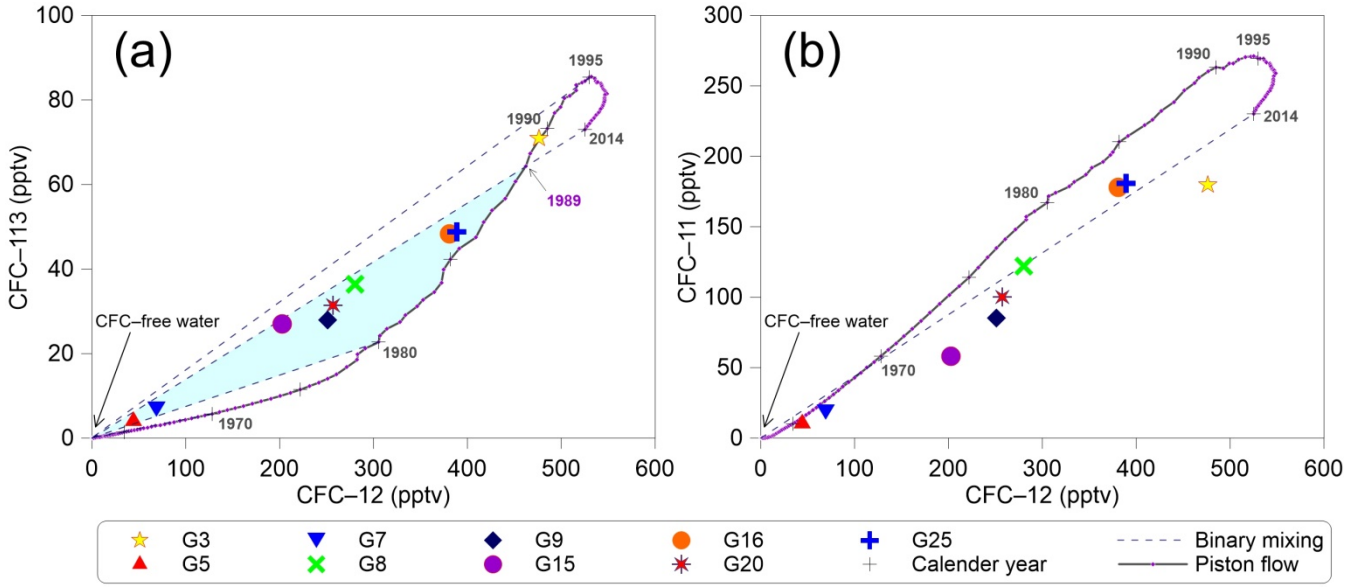

790 **Figure 7.** Plots showing relationships of (**a**) CFC–113 vs. CFC–12 and (**b**) CFC–11 vs. CFC–12 in pptv for the Northern Hemisphere air. The '+' denotes selected calendar years. The solid lines correspond to the piston flow and the short–dashed lines show the binary mixing. The shaded regions in (**a**) indicate no post–1989 waters mixing.

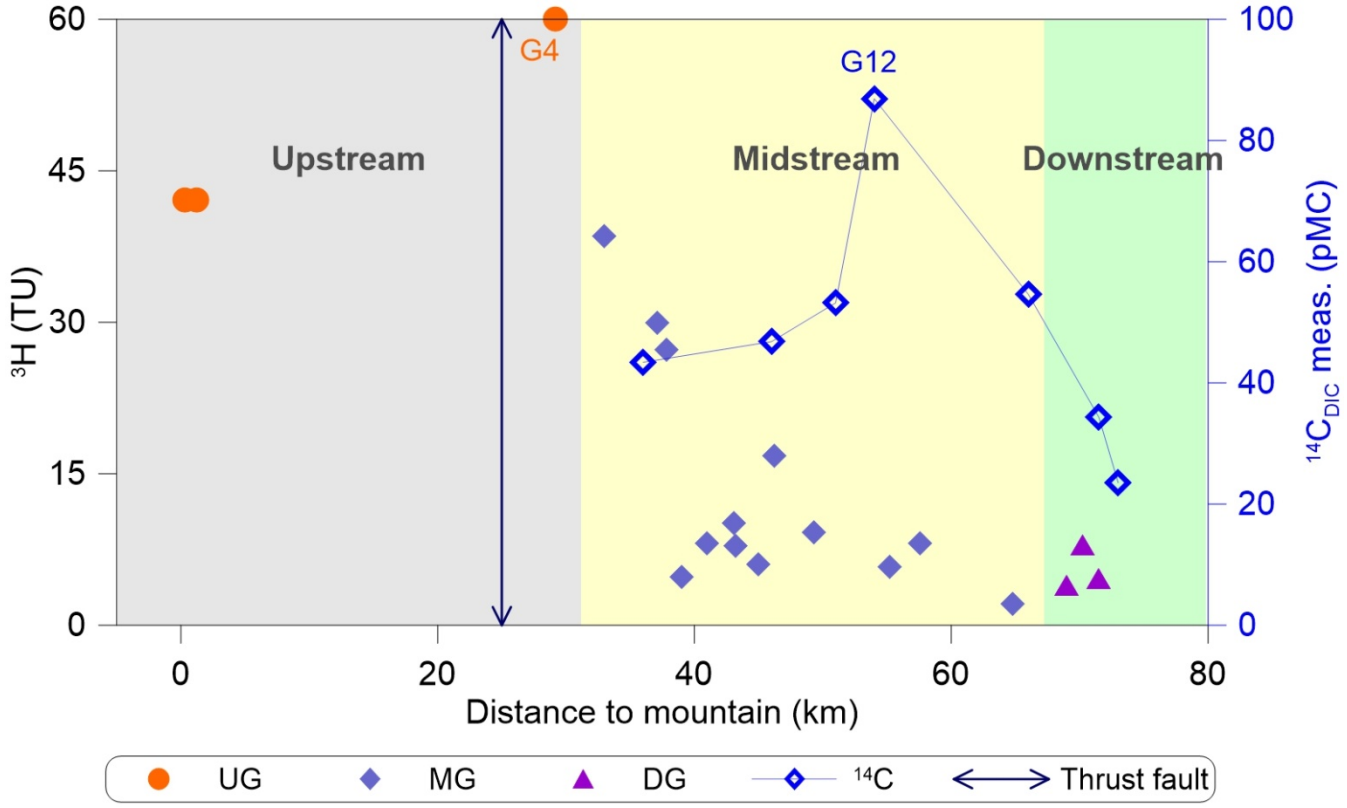

795 **Figure 8.** Distributions of ^{3}H and ^{14}C activities with distance to mountain. The shaded regions indicate the upstream, midstream and downstream of Manas River.

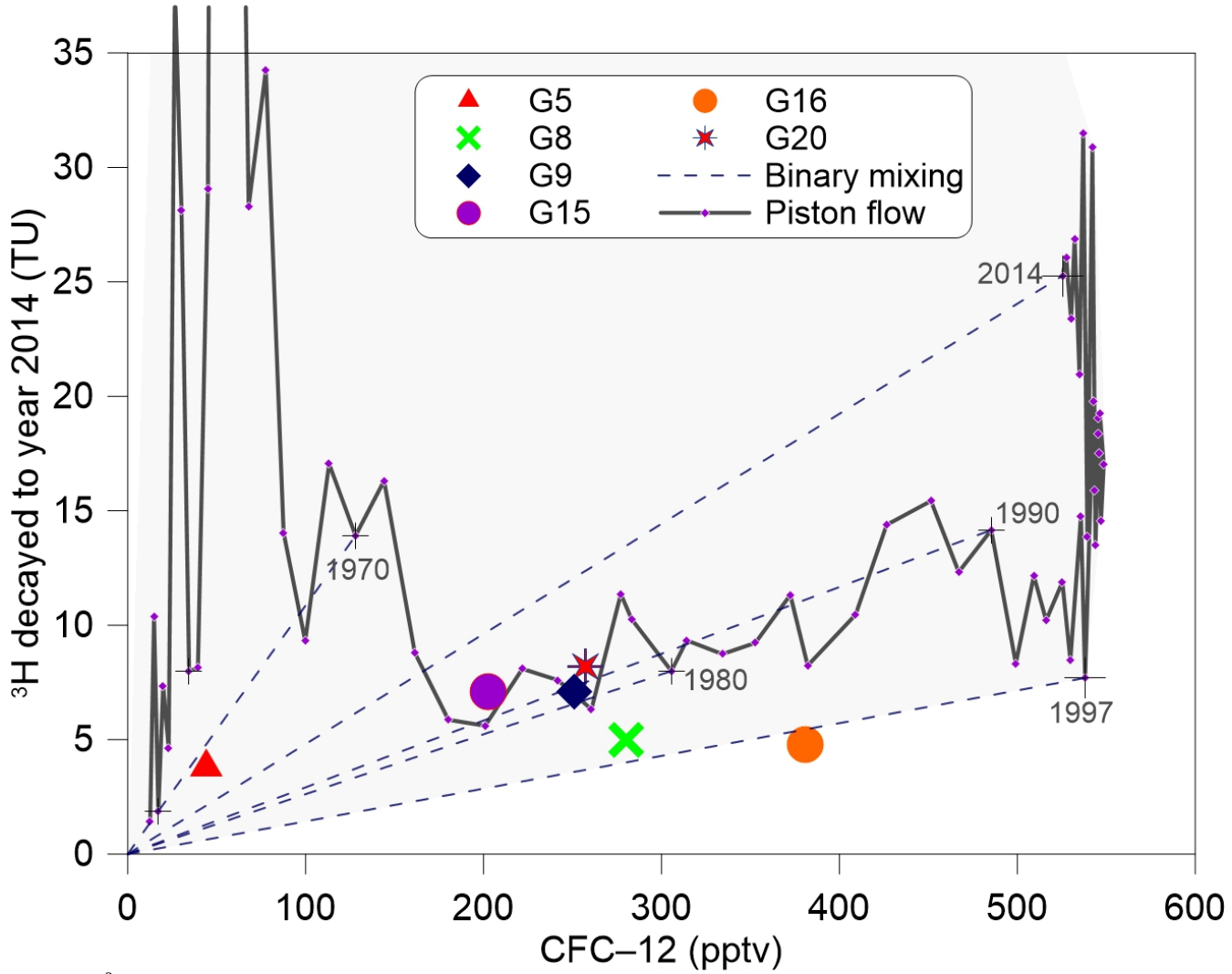

Figure 9. ^{3}H activity (TU) in Urumqi precipitation decayed to 2014 vs. CFC–12 in pptv for Northern Hemisphere air. The '+' denotes selected calendar years. The solid lines correspond to the piston flow and the short–dashed lines show the binary mixing. The shaded region indicates concentrations that could arise due to mixing water of different ages.

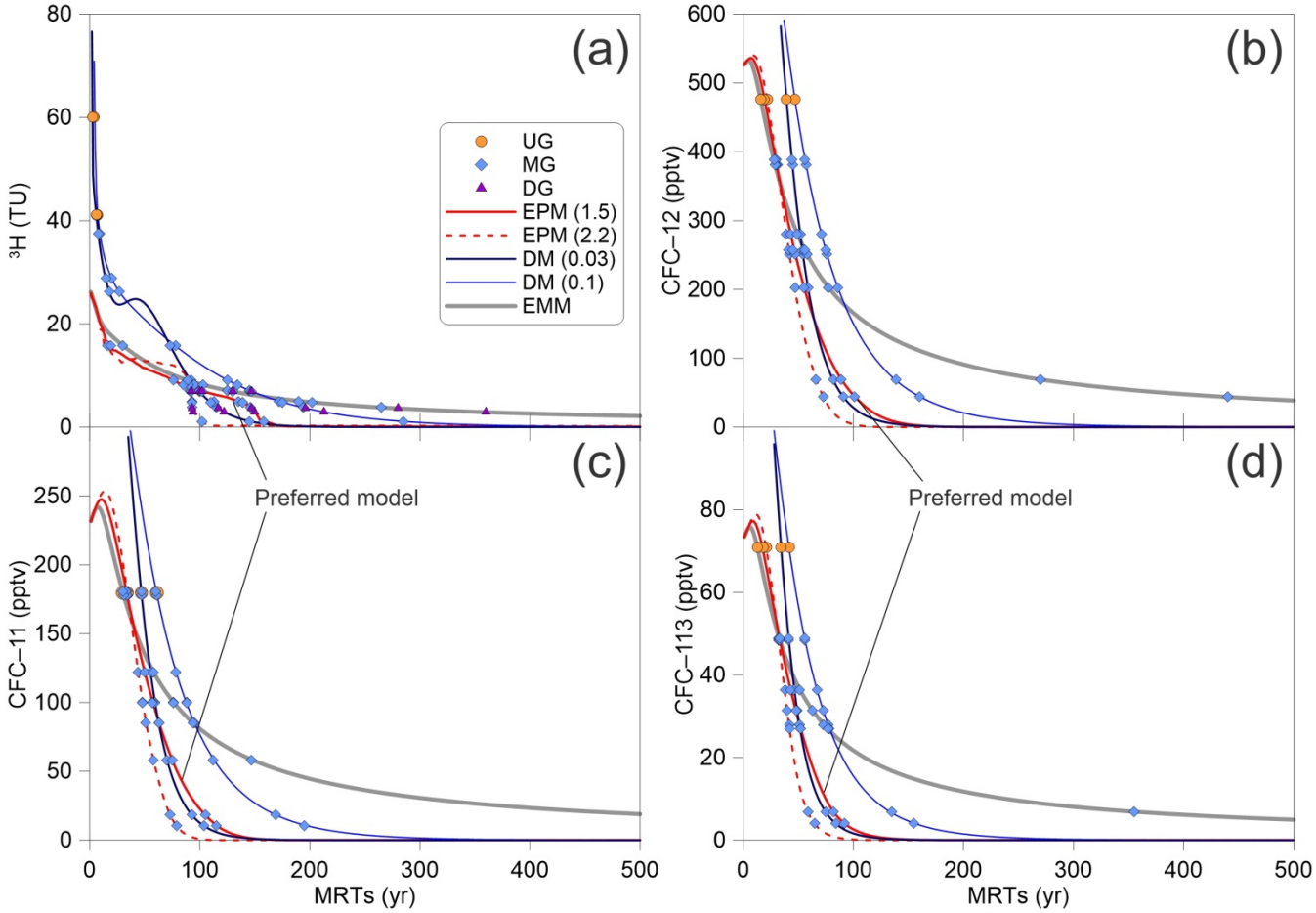

Figure 10. Tritium and CFCs (CFC–11, CFC–12 and CFC–113) output vs. mean residence times for different lumped–parameter models estimated using Eqs. (2) to (5). The input ^{3}H activity and CFCs concentration are using the estimated ^{3}H activity in precipitation in Urumqi station (Fig. 4) and the Northern Hemisphere atmospheric mixing ratio (Fig. 3), respectively.

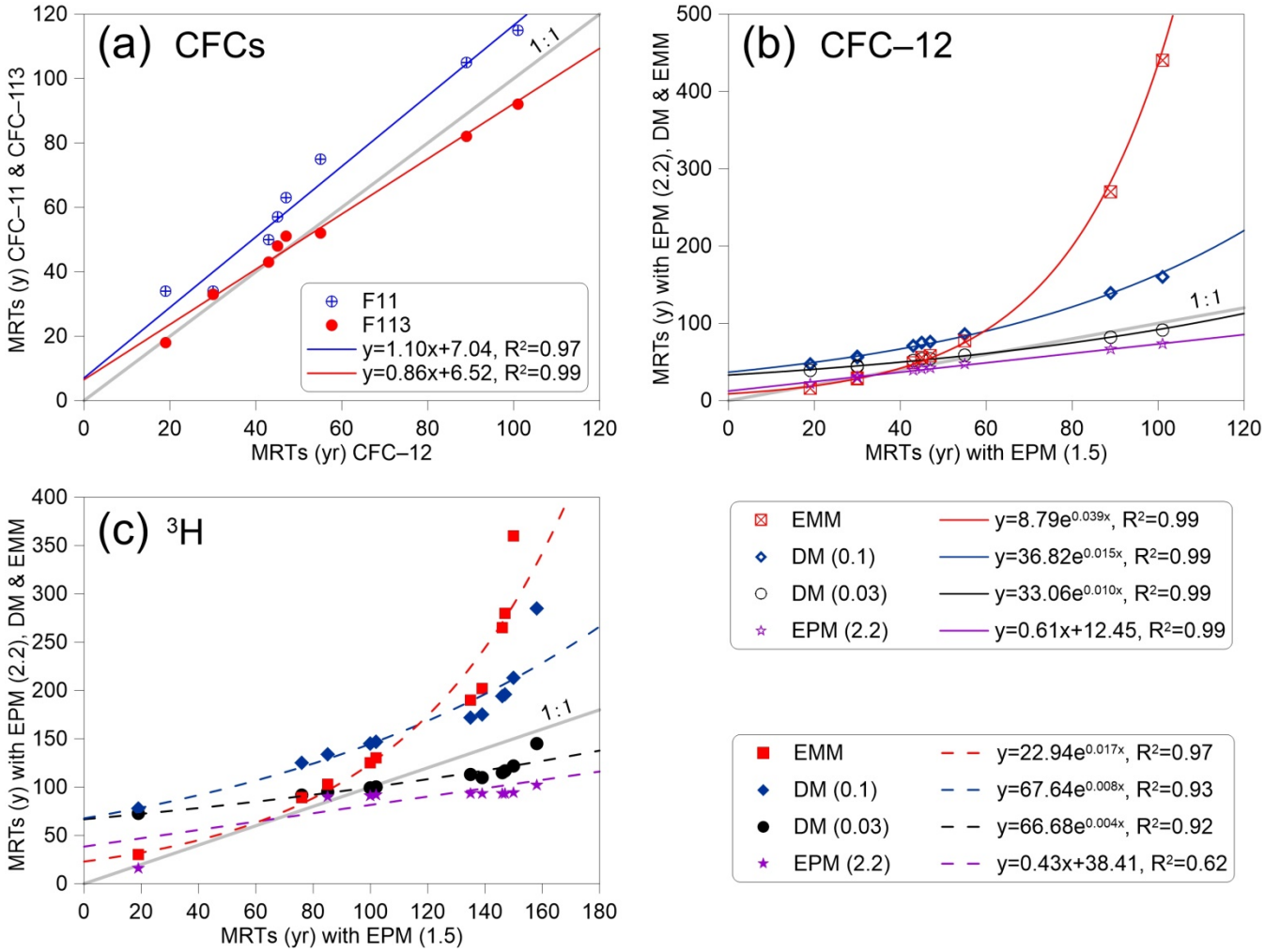

Figure 11. (**a**) MRTs with EPM (1.5) of CFC–12 vs. CFC–11 & CFC–113, (**b**) CFC–12 MRTs with EPM (1.5) vs. EPM (2.2), DM & EMM, and (**c**) 3H MRTs with EPM (1.5) vs. EPM (2.2), DM & EMM.

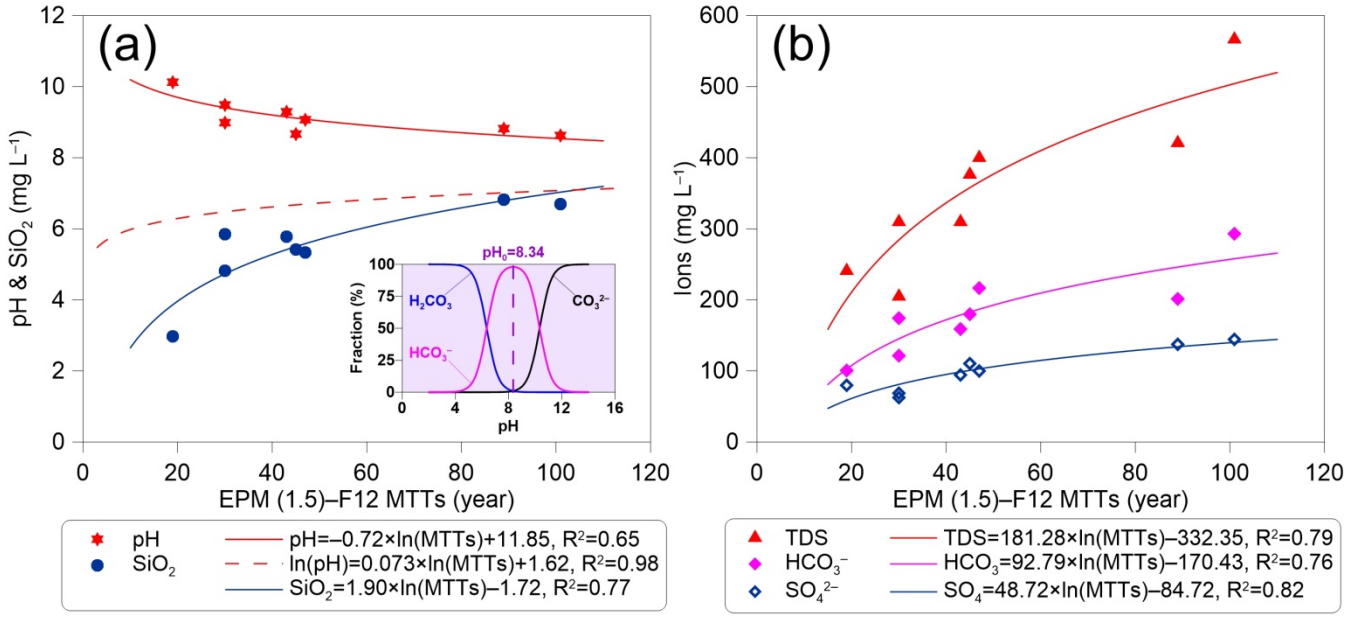

Figure 12. (**a**) pH & silica (SiO_2) and (**b**) ions including sulfate (SO_4^{2-}), bicarbonate (HCO_3^-), and total dissolved solids (TDS) vs. EPM (1.5)–F12 MRTs (CFC–12 MRTs using EPM (1.5)). The dashed red line in (**a**) is from Morgenstern et al. (2015).